Contents lists available at ScienceDirect

Thin-Walled Structures

A tensegrity structure for a solar stadium roof with sun-tracking capability

Rana Nazifi Charandabi [a] , Enrico Babilio [b] , Gerardo Carpentieri [c] , Giovanni Spagnuolo [a] ,
Ada Amendola [c] , Fernando Fraternali [c],*

[a] *Department of Information Engineering, Electrical Engineering and Applied Mathematics (DIEM), University of Salerno, Via Giovanni Paolo II 132, 84084 Fisciano (Salerno), Italy*
[b] *Department of Structures for Engineering and Architecture (DiSt), University of Naples "Federico II", Via Forno Vecchio 36, 80134 Naples, Italy*
[c] *Department of Civil Engineering, University of Salerno, Via Giovanni Paolo II 132, 84084 Fisciano (Salerno), Italy*

ARTICLE INFO

ABSTRACT

This work presents a tensegrity design approach for a small-to-medium-sized sports stadium, equipped with sun-tracking solar modules on its roof. A novel V-Expander unit is used to create a modular roof structure, with members optimized using a minimal mass strategy. The stability of the entire stadium structure and the deflections of the cantilever roof are analyzed under vertical, seismic, and wind loads through detailed finite element analysis. Electrical power production is estimated over one year for the Salerno area. The results demonstrate that the tensegrity solar roof exhibits limited deflections and remarkable solar energy harvesting capabilities, utilizing sun-tracking strategies tailored to different sectors of the grandstands. This research paves the way for the design of multi-scale sports stadiums featuring sustainable, adaptive lightweight tensegrity structures. These systems employ sun-tracking photovoltaic modules that can be tilted by simply wrapping a bus cable around a winch.

1. Introduction

Architects, engineers, and sports agencies have been working for over 20 years to enhance the sustainability of sports stadiums and reduce their energy consumption and carbon footprint, which are typically very high [1–3]. In most modern stadiums, a significant amount of energy is needed during matches to power advertising boards, lighting, air conditioning, ventilation in enclosed spaces, and other electrical services. These substantial energy demands contribute to the considerable carbon footprint of sports stadiums, which is further exacerbated by the use of energy-intensive materials and construction systems [4]. The Fédération Internationale de Football Association (FIFA) launched the 'Green Goal' initiative in 2006 to reduce the carbon footprint of World Cup™ tournaments and other international soccer events. This program includes several measures, such as optimizing energy consumption, reducing waste, and using renewable energy sources [5].

A remarkable number of sports stadiums equipped with photovoltaic (PV) panels (solar-powered stadiums) have been designed and built in recent years (see, e.g., the statistics presented in [2]). There are large-scale projects, such as the Garrincha Stadium in Brasília, Brazil, which is equipped with 9600 PV panels and produces a peak electrical power of 2500 kWp, as well as the Bentegodi Stadium in Verona, Italy (13 300 PV panels, 1000 kWp) and the National Stadium in Kaohsiung, Taiwan (8844 PV panels, 1000 kWp). Medium-sized projects include

the Kyocera Stadium in The Hague, The Netherlands, with 2900 PV panels generating 725 kWp, while smaller-scale installations include the Euroborg Stadium in Groningen, The Netherlands, with 1100 PV panels producing 273 kWp. Efficient, solar-powered stadiums can produce a significant energy surplus—ranging from 1500 to 5000 MW h per year—beyond the energy required for their own operation [6].

The interesting study presented in [7] reports that a medium-sized stadium can exhibit energy consumption during a sporting event on the order of 10 000 MW h per year, corresponding to carbon dioxide emissions of 3600 tonnes annually. The same reference highlights that the energy consumption of the stadium used for the US Super Bowl is comparable to that of an entire African country, reaching up to 10 MW h during operation. It is worth noting that solar thermal panels provide a valid alternative or complement to PV panels in hot and humid climates with high peak temperatures [7]. The dragon's tail shape of the Kaohsiung Stadium allows for a smoothly variable orientation of the PV panels along the length of the roof. This design is beneficial for aesthetic reasons and also for optimizing solar energy gain by adjusting the panels' orientation [8]. Recently, a retractable solar roof equipped with 10 414 PV panels (4200 kWp) was installed at the Galatasaray Stadium in Istanbul, Turkey [9]. However, it appears that no examples of stadium roofs with sun-tracking PV panels have been realized to

---

date.

Sustainable stadiums need to be lightweight and structurally stable while also being energy-efficient [10]. Tensegrity structures, which offer a unique lightweight structural typology, have been demonstrated by Robert E. Skelton and several collaborators to provide minimal mass solutions for a variety of loading conditions in recent years (see, for example, [11–13]). Such structural systems resist external loads with pure axial forces in their members, which consist of either compressed struts or bars and stretched (most often prestressed) cables or strings [13]. It is often believed that tensegrity structures possess low stiffness due to the fact that the struts are not connected to each other and the presence of infinitesimal mechanisms [14]. While this is true for classical class-1 tensegrities (where only one bar is attached to each node), it has been shown that high-stiffness properties can be achieved in tensegrity systems through optimized geometries and topologies, the use of class-k configurations (where the maximum number of bars attached to nodes is k), and appropriate prestress strategies [13,15]. Tensegrity or tensegrity-inspired architectures have been employed in the design of bridge structures [12], the Georgia Dome stadium in Atlanta, Georgia, USA (demolished in 2017), and the La Plata Stadium in Buenos Aires, Argentina, to name a few examples of such structural systems used in civil engineering [14,16,17].

The present study illustrates the tensegrity design of a novel solar stadium structure with sun-tracking capabilities. A suitable variant of one of the V-Expander modules proposed in [18] is used. The class-4 tensegrity system employed for the stadium roof is described in Section 2, which details the prestress modes of the structure and the minimal mass design conducted using the strategy outlined in [11,12]. The overall architectural design of the examined tensegrity stadium is presented in Section 3. A comprehensive finite element analysis of the structural response of one sector of the stadium's grandstands to gravity, wind forces and seismic forces is provided in Section 4. The solar energy harvesting capacity is explored in Section 5, which discusses the sun-tracking abilities of the triangular PV modules forming the solar roof and calculates the overall electrical energy produced in one year at the site in Salerno, Italy. Concluding remarks and directions for future work are presented in Section 6.

2. Tensegrity roof module

The stadium roof structure examined in this work tessellates the novel V-Expander tensegrity unit, as illustrated in Fig. 1, to form the roof elements of the grandstand structures described in the following sections. The original V-Expander was introduced by René Motro in his well-known textbook [19] as a V-shaped system composed of eight bars arranged in two distinct sets of four bars each, with equal lengths. The bars are connected by one vertical cable, along with eight horizontal and eight diagonal cables (see also [18,20,21]). We examine a modification of the fifth variant ('Variant V') of the V-Expander cell proposed in [18] (see also [22]). This variant is a class-4 tensegrity structure composed of eight bars and seven cables. However, the system examined in this work and shown in Fig. 1 differs in the arrangement of cables and bars compared to the Variant V studied in [18,22]. It features a vertical quadrangular section with height h and width d, formed by nodes 1, 2, 3, and 5, as shown in Fig. 1. The system is completed by one base triangle (1, 4, 6) lying in a horizontal plane and a sloped triangle (2, 4, 6). The 'arms' 1–4 and 1–6 lie on a circle with radius r, centered at node 1. The module depicted in Fig. 1 is used in this work to create a cantilever roof structure by arranging an array of modules along the y-axis, which is perpendicular to the x-axis aligned with the bar 1–3. Our tensegrity stadium concept assumes the y-axis is parallel to one edge of the grandstands, which form a sports stadium structure with a rectangular plan (see Section 3). It is easily demonstrated that the module in Fig. 1 does not exhibit infinitesimal mechanisms. We align the z-axis with the bar 1–2 and set the origin of the $\{x, y, z\}$ Cartesian
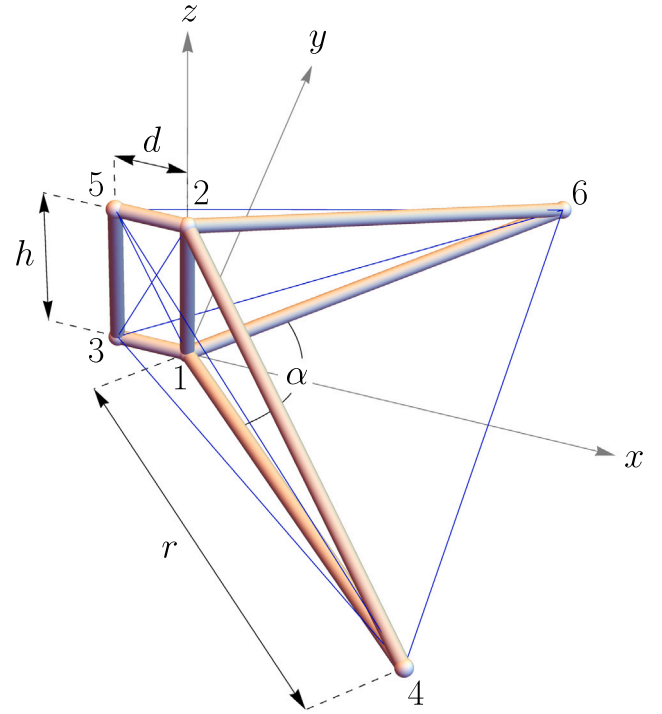

Fig. 1. Examined V-Expander unit.

coordinate system at node 1. It is worth noting that the V-Expander module designed for minimal mass is modeled as an independent structure with restraint conditions to simplify its interactions with adjacent parts of the grandstand structures presented in the following section. It is restrained by fixing node 3, constraining nodes 1, 2, and 5 in the longitudinal (y) direction, and additionally constraining node 1 in the vertical (z) direction. The prestress modes applicable to this system are described below.

2.1. Prestress modes

Let x denote the vector of the *force densities* in the bars and cables, which are defined as the ratios between the axial forces t_{b_i} and t_{s_i} carried by these members and the corresponding lengths b_i and s_i. We assume that such quantities are positive when in tension for the cables and positive when in compression for the bars. Additionally, we order the elements of x by first listing the seven force densities in the cables 3–4, 4–6, 6–3, 4–5, 5–6, 5–1, and 3–2, followed by the eight force densities in the bars 1–2, 5–3, 1–4, 1–6, 2–4, 2–6, 2–5, and 1–3. We let $M = 15$ denote the total number of members and $N = 6$ the number of nodes of the V-Expander module. The equilibrium equations of the structure can be cast into the following matrix form

$$Ax = w \tag{1}$$

where A is the $3N \times M$ *equilibrium matrix*, $x \in \mathbb{R}^M$ if the force density vector, and $w \in \mathbb{R}^{3N}$ is the *nodal force vector* of the system ($\mathbb{R}$ denotes the set of real numbers). The qth member of the structure contributes to the rth equilibrium equation of the pth node ($r = 1, 2, 3$ corresponding to the equilibrium equations along the x, y and z axes, respectively) with the opposite of the rth component of the vector defined by the difference between the position vector of node p and the position vector of the other node connected by this member. We are assuming the qth member is connected to node p; otherwise, this member does not contribute to the equilibrium equations of node p.
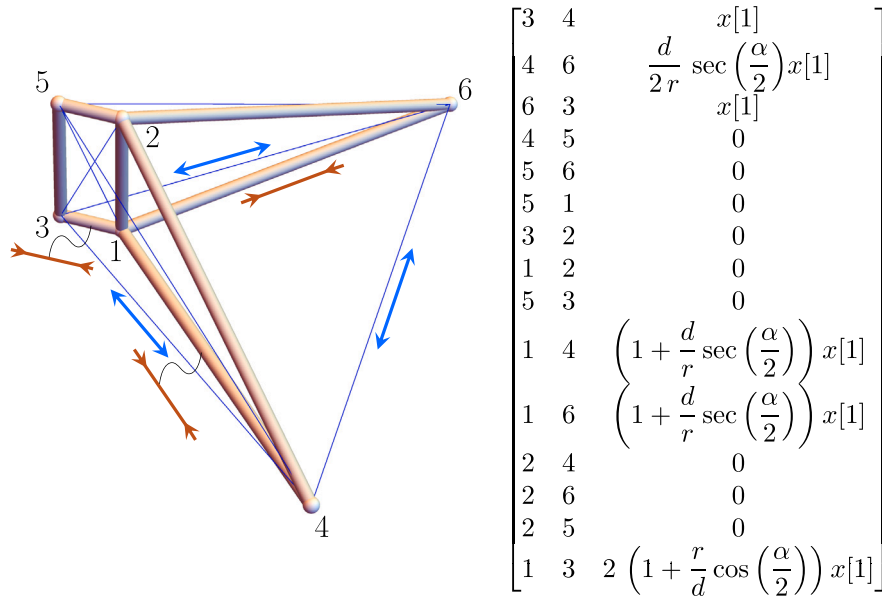
$$\begin{bmatrix} 3 & 4 & x[1] \\ 4 & 6 & \dfrac{d}{2\,r}\,\sec\left(\dfrac{\alpha}{2}\right)x[1] \\ 6 & 3 & x[1] \\ 4 & 5 & 0 \\ 5 & 6 & 0 \\ 5 & 1 & 0 \\ 3 & 2 & 0 \\ 1 & 2 & 0 \\ 5 & 3 & 0 \\ 1 & 4 & \left(1+\dfrac{d}{r}\,\sec\left(\dfrac{\alpha}{2}\right)\right)x[1] \\ 1 & 6 & \left(1+\dfrac{d}{r}\,\sec\left(\dfrac{\alpha}{2}\right)\right)x[1] \\ 2 & 4 & 0 \\ 2 & 6 & 0 \\ 2 & 5 & 0 \\ 1 & 3 & 2\left(1+\dfrac{r}{d}\,\cos\left(\dfrac{\alpha}{2}\right)\right)x[1] \end{bmatrix}$$

Fig. 2. Prestress mode that is produced by stretching the cables in the base triangle 3-4-6 (mode #1). Force vectors colored blue indicate tensile prestress forces in the cables, while force vectors colored brown indicate compressive prestress forces in the bars. The matrix shown on the right specifies the force density acting on the generic member with end nodes i and j.

The prestress (or *self-stress*) modes of the structure correspond to the non-trivial solutions of Eq. (1) when $w = 0$, that is, in the absence of external forces. Simple algebraic computations demonstrate that the V-Expander module under examination exhibits prestress modes generated by linear combinations of the three base modes illustrated in Figs. 2, 3, and 4. The mode shown in Fig. 2 is modulated by the force density $x[1]$ in the cable 3–4 of the base triangle 3-4-6 (which coincides with the force density in the cable 6–3). In contrast, the mode depicted in Fig. 3 is modulated by the force density $x[4]$ in the cable 4–5 of the sloped triangle 5-4-6 (coinciding with the force density in the cable 5–6). Finally, the mode depicted in Fig. 4 is modulated by the force densities acting in the cables 3–2 ($x[6]$) and 5–1 of the vertical section of the module.

2.2. Minimal mass design procedure

We carry out a minimal mass design of the V-Expander module, as described in the previous section, utilizing the iterative linear programming procedure outlined in [11]. For a single loading condition, this procedure is formulated as the following minimization problem

$$\underset{x}{\text{minimize}} \quad m = c^T x \tag{2}$$

$$\text{subject to} \quad \begin{cases} Ax = w \\ x \geq 0 \end{cases}$$

where

$$c = \left(\begin{array}{ccc|ccc} \dfrac{\rho_b b_1^2}{\sigma_{b_1}} & \cdots & \dfrac{\rho_b b_{n_b}^2}{\sigma_{b_{n_b}}} & \dfrac{\rho_s s_1^2}{\sigma_{s_1}} & \cdots & \dfrac{\rho_s s_{n_s}^2}{\sigma_{s_{n_s}}} \end{array} \right)^T . \tag{3}$$

Here, m denotes the overall mass of the system; ρ_b and ρ_s represent the mass densities of the n_b bars and n_s cables, respectively; b_i^2 and s_i^2 indicate the squares of the lengths of such members. The design stress of the ith bar is denoted as σ_{b_i} ($i = 1, \dots, n_b$), and that of the ith cable as σ_{s_i} ($i = 1, \dots, n_s$). Hereafter, we utilize the generalization of the problem (2) to multiple loading conditions, as detailed in [11], to which we direct the reader for further information. Initially, we assume that all cables and bars exhibit circular cross-sections and are made of steel with a mass density of $7862\,\mathrm{kg\,m^{-3}}$. For the bars, the material

Table 1
Nodal forces generating the loading conditions analyzed in the minimal mass design procedure. Nodes 3 and 5 are assumed to be at rest; node 1 is constrained in the x direction.

combination	node	$F_x = F_y$	F_z
		(kN)	(kN)
1) dead loads	2	0	−69 328
	5	0	−11 702
	4, 6	0	−57 626
2) dead loads + wind downward	2	−37 647	−225 217
	5	0	−39 812
	4, 6	−37 647	−185 405
3) dead loads + wind upward	2	37 647	86 561
	5	0	16 408
	4, 6	37 647	70 153

properties include a Young's modulus $E_b = 206 \times 10^9\,\mathrm{N\,m^{-2}}$ and a yield stress $\sigma_Y = 223 \times 10^6\,\mathrm{N\,m^{-2}}$. For the cables, the material properties include a Young's modulus $E_s = 160 \times 10^9\,\mathrm{N\,m^{-2}}$ and a yield stress $\sigma_Y = 1200 \times 10^6\,\mathrm{N\,m^{-2}}$, as specified by the manufacturer of the spiral strand steel wire ropes, Sirtef srl [23]. The examined roof module has dimensions of $r = 12\,\mathrm{m}$, $h = 5\,\mathrm{m}$, and $d = 2\,\mathrm{m}$.

Use is made of design stresses $\sigma_{s_i} = \sigma_Y$ in all the cables and design stresses $\sigma_{b_i} = \min\{\sigma_Y, \sigma_{B_i}\}$ in the bars. Here, σ_{B_i} indicates the buckling stress obtained by dividing the Euler buckling load in the ith bar by the cross section area of such a member [11]. The following 11 external load conditions are taken into consideration: dead loads; dead loads plus wind forces acting downward (i.e., in the negative z direction); dead loads plus wind forces acting upward (i.e. in the positive z direction); seismic loads acting in both x and y directions for a total of 8 seismic load cases. These loading conditions are generated by the nodal forces listed in Table 1. The reader is referred to Sections 3–4 for the derivation of the numerical values of the forces presented in Table 1 and seismic load cases.

The minimal mass design procedure returns the theoretical cross-sectional areas and radii of cables and bars, which are denoted by $A_{ij,th}$ and $r_{ij,th}$ in Tables 2 and 3, respectively. Such a design aims to achieve
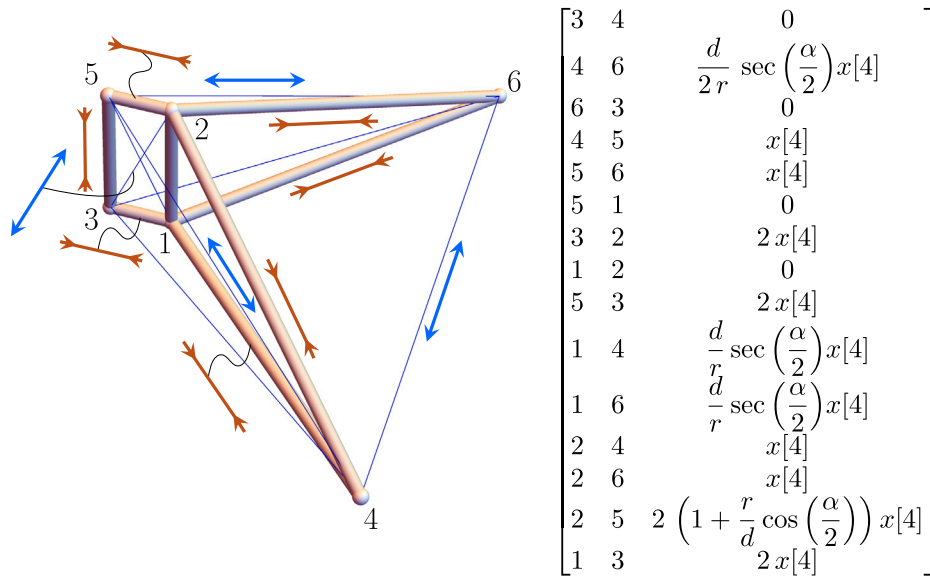
$$
\begin{bmatrix}
3 & 4 & 0 \\
4 & 6 & \dfrac{d}{2\,r}\sec\left(\dfrac{\alpha}{2}\right)x[4] \\
6 & 3 & 0 \\
4 & 5 & x[4] \\
5 & 6 & x[4] \\
5 & 1 & 0 \\
3 & 2 & 2\,x[4] \\
1 & 2 & 0 \\
5 & 3 & 2\,x[4] \\
1 & 4 & \dfrac{d}{r}\sec\left(\dfrac{\alpha}{2}\right)x[4] \\
1 & 6 & \dfrac{d}{r}\sec\left(\dfrac{\alpha}{2}\right)x[4] \\
2 & 4 & x[4] \\
2 & 6 & x[4] \\
2 & 5 & 2\left(1+\dfrac{r}{d}\cos\left(\dfrac{\alpha}{2}\right)\right)x[4] \\
1 & 3 & 2\,x[4]
\end{bmatrix}
$$

Fig. 3. Prestress mode generated by stretching the cables of the sloped triangle 5-4-6 (mode # 2).

$$
\begin{bmatrix}
3 & 4 & 0 \\
4 & 6 & 0 \\
6 & 3 & 0 \\
4 & 5 & 0 \\
5 & 6 & 0 \\
5 & 1 & x[6] \\
3 & 2 & x[6] \\
1 & 2 & x[6] \\
5 & 3 & x[6] \\
1 & 4 & 0 \\
1 & 6 & 0 \\
2 & 4 & 0 \\
2 & 6 & 0 \\
2 & 5 & x[6] \\
1 & 3 & x[6]
\end{bmatrix}
$$
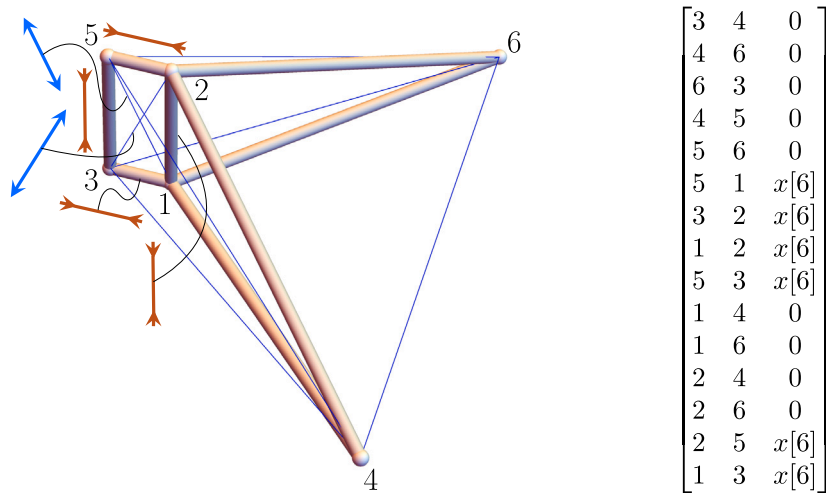
Fig. 4. Prestress mode generate by stretching the cables of the vertical section of the module (mode # 3).

an initial gross sizing of the members forming the V-Expander module. To standardize the scattered outputs and align them with the finite element analysis presented in Section 4 (considering various levels of prestress), we utilized spiral strand steel wire ropes supplied by Sirtef srl [23]. These ropes, manufactured from harmonic high-strength steel wires, have a diameter of 57 mm and a minimum breaking force (MBF) of 2610 kN for all cables. Similarly, steel profiles with cold-formed square hollow sections (HS) [24], characterized by a 400 mm edge and 16 mm thickness, were used for all bars.

3. Tensegrity stadium concept

We examine a stadium structure composed of four independent grandstands: two 'long' grandstands with a longitudinal span of 101.82 m, and two 'short' grandstands with a span of 67.88 m (Figs. 5–6).

The four grandstands are assumed to be positioned along the edges of the stadium, with each aligned to a different cardinal direction. The two long grandstands are situated along the north and south edges,

Table 2
Theoretical and regularized dimensions of the cables obtained through the minimal mass design procedure. Here, i and j denote the endpoint nodes of the generic cable, $A_{ij,th}$ and $\curlyvee_{ij,th}$ represent its theoretical cross-sectional area and theoretical radius, respectively.

i	j	$A_{ij,th}$ (m^2)	$\curlyvee_{ij,th}$ (mm)
3	4	3.29×10^{-4}	10.24
4	6	1.12×10^{-4}	5.98
6	3	3.29×10^{-4}	10.24
4	5	4.88×10^{-4}	12.46
5	6	4.88×10^{-4}	12.46
5	1	4.31×10^{-4}	11.72
3	2	1.80×10^{-3}	23.91

while the two short grandstands are located along the east and west edges (Fig. 5). The grandstands reach a total height of 20 m up to the
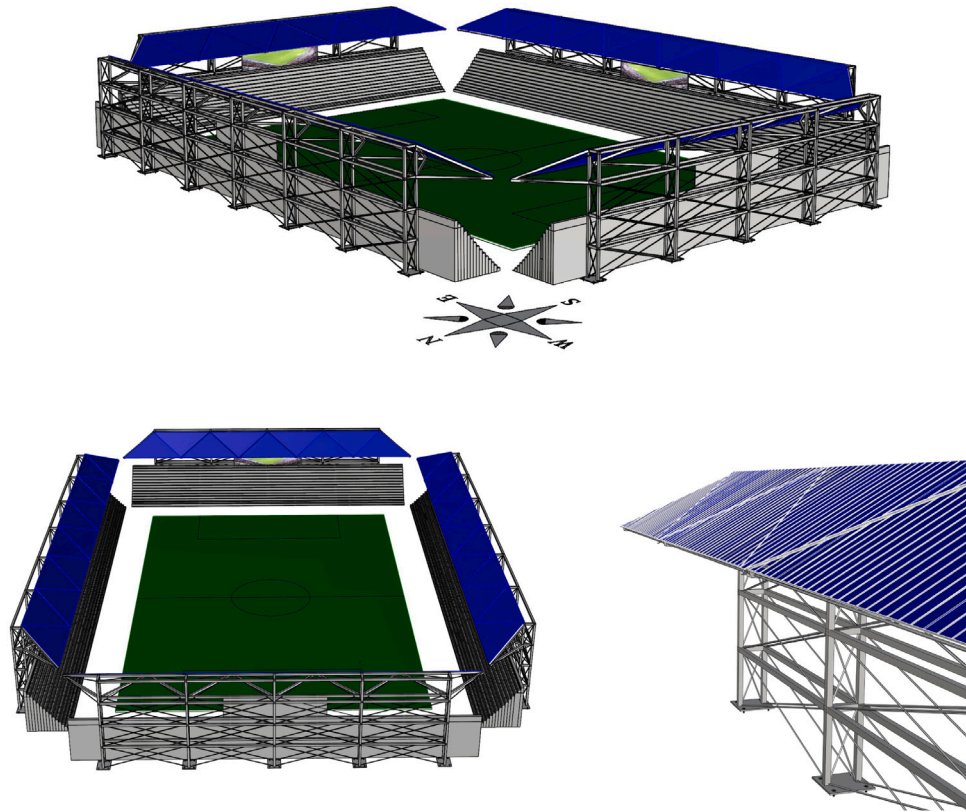
Fig. 5. Axonometric (top), aerial (bottom-left), and close-up roof (bottom-right) views of the solar stadium structure analyzed in this study, highlighting the roof covered with strips of lightweight, flexible, thin-film PV cells. The stadium comprises two 'long' grandstand sections along the south and north sides, parallel to the longer edges of the rectangular field, and two 'short' grandstand sections along the east and west sides, parallel to the shorter edges of the field.

Table 3
Theoretical and regularized dimensions of bars obtained through the minimal mass design procedure. In this table, i and j denote the endpoint nodes of the generic bar. The quantity $A_{ij,th}$ represents the theoretical cross-sectional area of the bar, while $\curvearrowright_{ij,th}$ denotes the theoretical radius of the circular cross-section.

i	j	$A_{ij,th}$ (m²)	$\curvearrowright_{ij,th}$ (mm)
1	2	1.94×10^{-2}	78.64
5	3	8.50×10^{-3}	52.00
1	4	2.55×10^{-2}	90.10
1	6	2.55×10^{-2}	90.10
2	4	1.19×10^{-2}	61.47
2	6	1.19×10^{-2}	61.47
2	5	4.79×10^{-3}	39.04
1	3	5.05×10^{-3}	40.11

axis of the top structural members and are composed of adjacent V-Expander roof modules (Section 2). These modules are mounted on vertical posts connected by two grids of bars and cables lying on parallel vertical planes (Fig. 6).

The short grandstands consist of four bays, each measuring 16.97 m, while the long grandstands consist of six bays of the same length (Fig. 6). The total seating capacity is estimated at nearly 10 000 seats (specifically 9800). This estimate considers a step tread of 0.60 m, a riser height of 0.60 m, a seat pitch of 0.45 m, 14 tiers, six stairways with a width of 1.20 m in the long grandstand sections, and four stairways in the short grandstand sections [25,26]. As a follow-up to the study presented in Section 2.2, we use the same elements, with material properties derived from Sirtef srl [23] and a diameter of 57 mm, for all cables in the overall stadium structure. For all the bars shown in Fig. 6, we use cold-formed steel HS sections with a 400 mm edge and a 16 mm thickness [24].

The pitched roof modules are constructed from standing seam metal roofing panels, with an overall height of 220 mm, a thickness of 4 mm,

and a self-weight of 486 N m⁻² (corresponding to a specific weight of 77.126 kN m⁻³). The triangular metal roofing modules are covered with strips of lightweight, thin, and flexible solar panels. These strips are attached to the upper sections of the corrugated roof modules, running along the roof's transverse direction (see Fig. 7). The solar panels have a self-weight of 44 N m⁻², including the self-weight of the scissor structure described later and a lightweight wire mesh backing. Their power conversion efficiency (PCE) ranges from 6% for amorphous thin-film cells [27] to 18% for organic PV panels [28], and up to 24% for flexible PV panels SunBender by Solbian, which encapsulate high-efficiency monocrystalline cells [29].

It is worth noting that roof panels have a nearly 30° slope in the reference configuration of the solar roof, measured with respect to the horizontal plane passing through the frontal longitudinal axis of the roof ('frontal' tilting angle: $\vartheta_0 = \arctan(h/(r\cos(\alpha/2))) = 0.532 \, \text{rad} = 30.509°$, cf. Section 2). Such initial slope can be varied by tilting the roof panels by a 'secondary' tilting angle $\hat{\vartheta}$ about the posterior longitudinal axis (one-axis tracking strategy), using a scissor-type tensegrity structure [30]. This structure consists of two struts with 300 mm HS sections (web thickness of 3 mm) that run beneath the roof panels. The struts are connected at their lower extremities to a looped bus cable, and at their upper extremities to hinges attached at the midpoints of two edges of the roof panel. The bus cable is also a spiral strand steel wire rope, similar to the other cables that form the stadium structure, but with a diameter of 30 mm. We refer the reader to Section 5 of [30] for a detailed description of the kinematics of the scissor tensegrity structure, which is graphically illustrated in Fig. 8. By wrapping the bus cable around an external winch, the struts rise from their initial position, tilting the roof panels and PV cells up to a (theoretical) maximum angle of $\hat{\vartheta}_{max} \approx 119°$. The study presented in Section 5 adopts a sun-tracking strategy in which all roof panels within an individual grandstand are uniformly tilted by a single secondary tilting angle $\hat{\vartheta}$ to prevent mutual
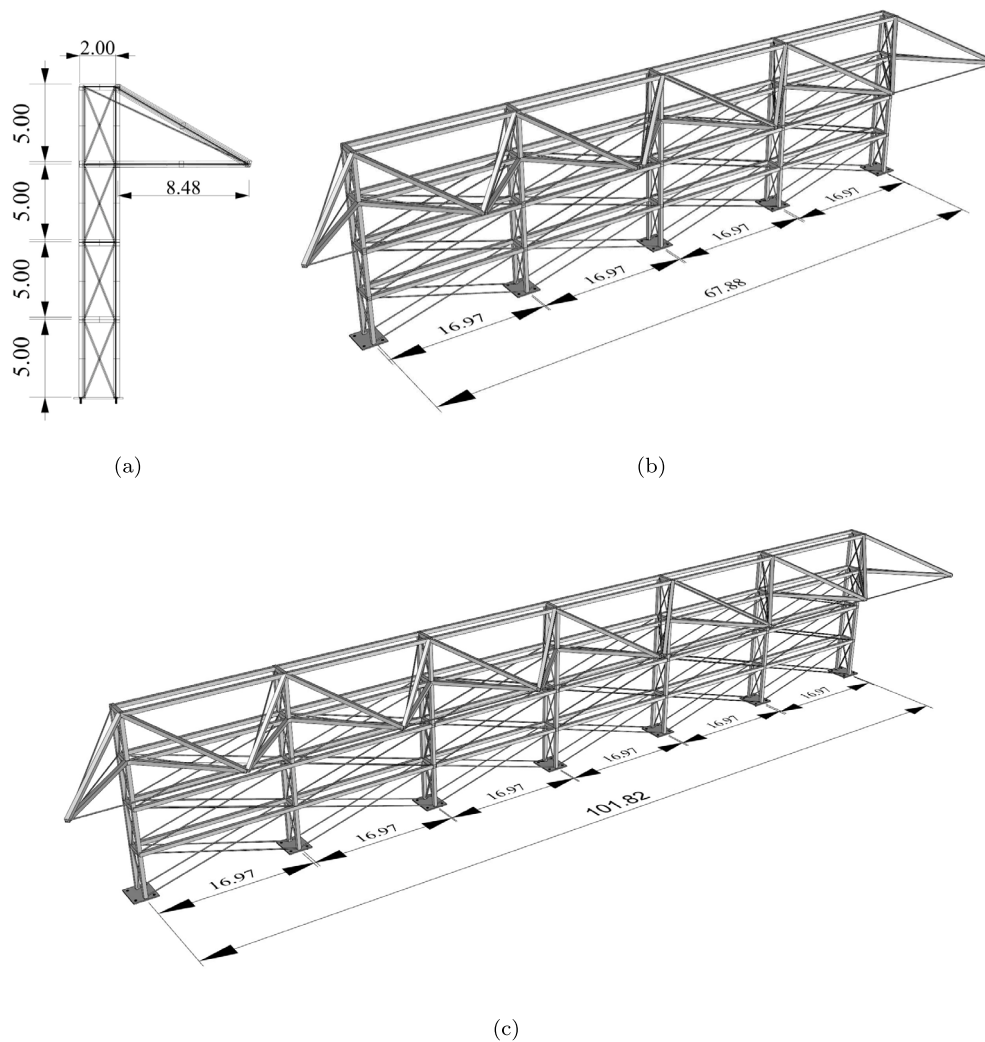
Fig. 6. Illustration of the grandstand sections of the stadium without roof plates and PV panels installed: (a) Detail of a post element; (b) Axonometric view of the structure of a short grandstand; (c) Axonometric view of the structure of a long grandstand section (dimensions in m).
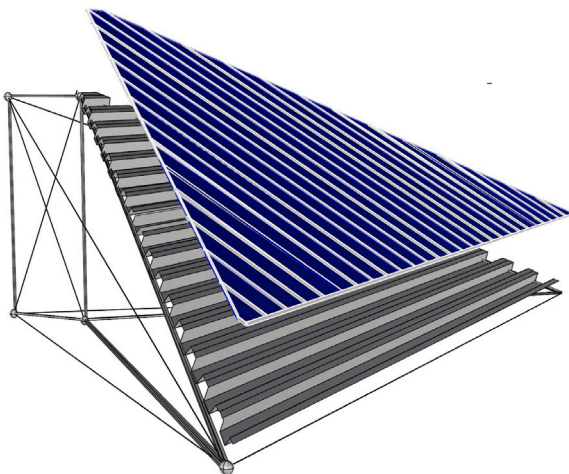

Fig. 7. Exploded view of a corrugated steel roof panel covered with thin-film PV strips. The supporting structure is shown in a schematic diagram for clarity of illustration.

shading, while allowing for varying angles $\hat{\vartheta}$ between the solar roofs of different grandstands (Fig. 9). The decision to implement additional tilting about the posterior axis, rather than rotation about the frontal axis, is guided by the aim of shifting the centers of mass of the tilted PV panels closer to the vertical supporting structure at the back of the V-Expander modules (Fig. 8), thereby improving the stability of the overall grandstand structure. This approach, however, constrains the PV panels to exhibit a constant value for the frontal tilting angle, as will be observed in the analysis presented in Section 5.

4. Finite element analysis

This section presents finite element (FE) simulations of a long grandstand section of the analyzed stadium, performed using the commercial software SAP2000® [31]. The analyzed model consists of 160 bars, 163 cables, and 78 joints. Specifically, the FE models used in Sections 4.1–4.2 employ frame elements with rotational releases at both ends for both bars and cables (see Fig. 10). The FEM models in Sections 4.3–4.4 instead use nonlinear link elements that carry only axial forces for the bars and cables. All the models introduce pinned joints at the base nodes.

We analyzed load cases corresponding to the effects of dead loads, wind loads, and seismic loads. An equivalent static lateral force approach was employed to model the effects of both wind and seismic
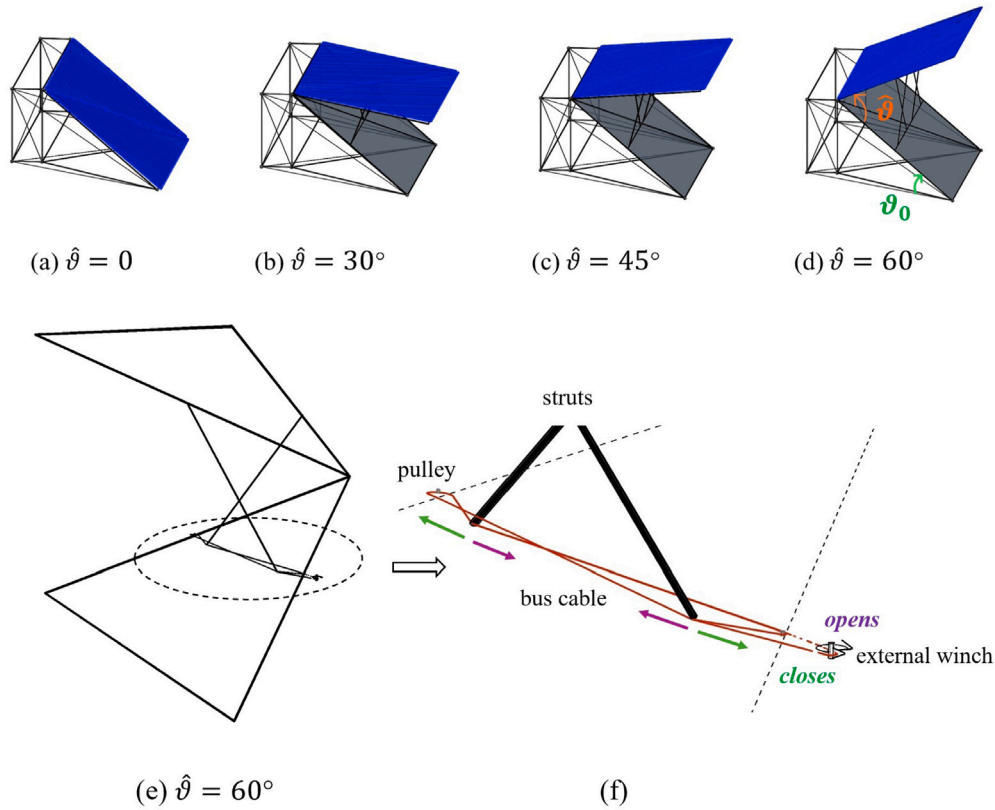
(a) $\hat{\vartheta} = 0$ (b) $\hat{\vartheta} = 30°$ (c) $\hat{\vartheta} = 45°$ (d) $\hat{\vartheta} = 60°$

(e) $\hat{\vartheta} = 60°$ (f)

Fig. 8. A cartoon illustrates the sun-tracking motion of a pair of roof panels at various secondary tilt angles $\hat{\vartheta}$ about the posterior longitudinal axis. Images (a)–(d) depict the roof panels in tilted configurations, with the reference configuration for $\hat{\vartheta} = 0$ represented as a hatched outline in images (b)–(d) for comparison. Images (e)–(f) show the external winch mechanism that drives the scissor structure to tilt a triangular roof panel.
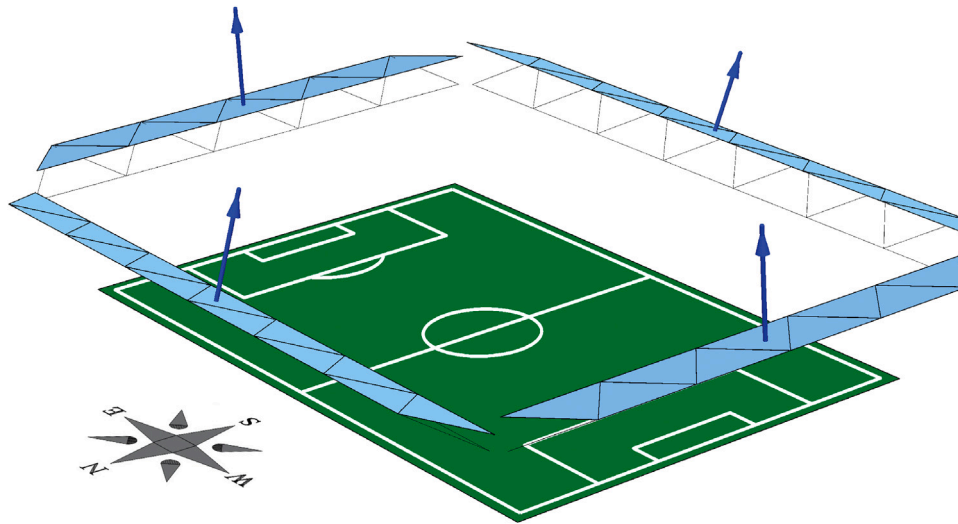
Fig. 9. Illustration of the sun-tracking strategy employed in the current stadium: the roof panels of the various grandstand sections are designed to tilt at distinct angles, maintaining uniform tilting within each section. The blue vectors indicate the normals to the tilted roof panels across the four grandstand sections.

forces, with design values specified according to the Italian structural code [32], which is inspired by Eurocodes 3 and 8 [33,34]. The site coordinates of the city of Salerno were used: Latitude: 40°40′31.62″ N and Longitude: 14°47′35.81″ E. The seismic forces were computed assuming a Peak Ground Acceleration (PGA) at the ultimate limit state (ULS) of 0.45 g, acting on a total mass of the structure of 13 500 kg plus the mass of the roof. The computed total seismic force was then distributed between all the structural nodes proportionally to their height and mass. Wind forces were assumed to act in the transverse

direction relative to the grandstand. We assume that the analyzed wind forces correspond to high or moderately high winds and that, as a result, the roof panels remain in the fixed-slope configuration (i.e., $\hat{\vartheta} = 0$) under the analyzed load combinations. This can be ensured by employing wind sensor anemometers to protect the roof from high or moderately high winds. The effects of wind and seismic forces on the roof configuration with tilted panels are left for future work. We considered two prestress cases generated by the pretension of cables 3–4 (prestress variable $x[1]$, see Section 2.1), 4–5 (prestress variable
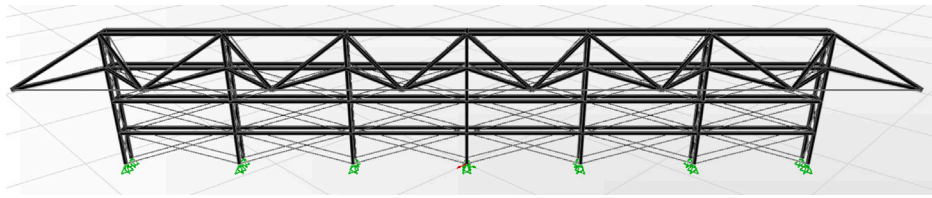
Fig. 10. FE model of a long grandstand section of the stadium. The green symbols indicate pinned joint restraints at the base.

Table 4
Load factors for the analyzed load combinations: G denotes the dead loads, P the prestress forces, W the wind forces, and E_x and E_y the seismic forces in the $x-$ (transverse) and $y-$ (longitudinal) directions. The coefficients c_x and c_y can take the values $1, -1, 0.3, -0.3$.

ultimate limit state	load combinations
'dead loads' ultimate limit state (DULS)	$1.3G$
	$1.3G + P$
'wind' ultimate limit state (WULS)	$1.3G + 1.5W$
	$1.3G + 1.5\ W + P$
'seismic' ultimate limit state (SULS)	$G + c_x E_x + c_y E_y$
	$G + c_x E_x + c_y E_y + P$

Table 5
Maximum vertical deflections of the terminal nodes in the cantilevered section of the V-Expander modules for the DULS and WULS load combinations.

Nodes	without prestress		with prestress	
	DULS (mm)	WULS (mm)	DULS (mm)	WULS (mm)
4, 6	63.15	101.36	61.91	85.45

$x[4]$), and 3–2 (prestress variable $x[6]$): zero pretension and pretension forces equal to 25% of the minimum breaking force of the cables, as specified by the manufacturer (MBF = 2610 kN) [23].

Fig. 11 illustrates the loads combinations considered in the finite element analysis. The loading conditions for dead loads, wind loads and seismic loads were modeled with external forces applied to the nodes of the structure, while the prestrain was modeled with an equivalent uniform distributed temperature assigned to the prestrained cables. We conducted a conventional ULS analysis, as required by the Italian code [32] (Section 4.1), along with two nonlinear push-over analyses [34] (Sections 4.3–4.4). The material properties described in Section 2.2 were used. For the pushover analyses, a yielding strain of 1% and an ultimate strain of 3.5% were applied to the cables. For the bars, we applied a compressive strength of 5260 kN, a yielding strain of 0.1%, and an ultimate strain of 3.5%.

4.1. Ultimate limit state analysis

The present analysis was conducted using the Nonlinear Static Analysis option in SAP2000®, accounting for material nonlinearities due to the tension-only response of the cables [31]. Load combinations defined by the Italian standard [32] were applied, as shown in Table 4, which introduces the symbols G, P, W, E_x, and E_y, representing the load conditions for dead load (self-weight of the structure plus the weight of the roof panels and PV strips), prestress forces, wind forces, seismic forces along the transverse x-axis, and seismic forces along the longitudinal y-axis, respectively. Two load combinations were used for the ULS analysis under dead loads (DULS), two for the ULS analysis with wind forces (WULS), and eight for the ULS analysis with seismic forces (SULS). The latter were obtained by allowing the coefficients c_x and c_y to take the values $1, -1, 0.3, -0.3$ as listed in Table 4.

The results presented in Figs. 12–13 show that the maximum tensile and compressive axial forces in the analyzed ULS combinations are lower than the compressive strength of the bars and the MBF of the cables, respectively. The compressive loads in the bars are also much lower than the corresponding Eulerian buckling loads. The minimum difference in absolute value between the current axial load and the buckling load in the bars was found to be equal to 43 629 kN (axial force equal to 1819 kN; buckling load equal to 45 448 kN; load combination: WULS with prestress).

4.1.1. Maximum deflections

We analyzed the maximum deflections of the terminal nodes in the cantilevered section of the V-Expander modules (specifically, nodes 4 and 6 in the most deformed module, as noted in Section 2), under the DULS and WULS load combinations. It was found that the SULS combinations produced lower deflection values compared to the WULS combinations. Fig. 14 illustrates the deformed shapes of the grandstand structure under WULS combinations (with and without prestress), while Table 5 presents the numerical values of the maximum observed deflections. To enhance the visualization of the deformed shapes, the actual displacements were multiplied by a magnification factor of 60 for both WULS combinations (with and without prestress). It can be observed that the maximum deflection of 101.36 mm for the WULS combination without prestress reduces to 85.45 mm when prestress is applied to the WULS combination, giving a 16% reduction due to a geometric stiffness effect [13]. It is worth comparing these deflection values with those reported in [10] for the following noticeable stadiums under similar DULS and WULS load combinations: CommBank Stadium (Sydney, Australia, 45 m span); Optus Stadium (Perth, Western Australia, 35 m span); and Lakhwiya Stadium (Doha, Qatar, 16 m span). These maximum vertical deflections were obtained in [10] through FE simulations: 194 mm for CommBank Stadium, 18 mm for Optus Stadium, and 142 mm for Lakhwiya Stadium. We observe that the present stadium exhibits significantly lower deflections compared to CommBank and Lakhwiya stadiums, especially in the presence of prestress loads. The case of Optus Stadium is special, as it features an optimized circular bowl layout, making it non-comparable to the present stadium, which is instead equipped with disconnected grandstand sectors. The stadium studied in this work has a layout and size very similar to Lakhwiya Stadium, which has a capacity of 10 000 seats and features a steel supporting structure weighing 800 tons [35], that is 8.00×10^5 kg in SI units. The current stadium's supporting structures have a total mass of 3.13×10^5 kg for a single long grandstand section, with an estimated total mass of approximately 10.56×10^5 kg for the structures forming all four grandstand sections. This represents a 24% increase in weight compared to the supporting structures of the lightweight Lakhwiya Stadium [10]. It is worth noting, however, that the Lakhwiya Stadium features a polyvinyl chloride (PVC)/polyester fabric roof [36], whereas the current stadium employs a steel roof. Moreover, the roof of the current stadium is designed to accommodate PV panels, unlike that of the Lakhwiya Stadium.

4.2. Global buckling analysis

We supplemented the study presented in Section 4.1 with a global buckling analysis conducted at the endpoints of the static analyses for the DULS, WULS, and SULS load combinations. For this task, we
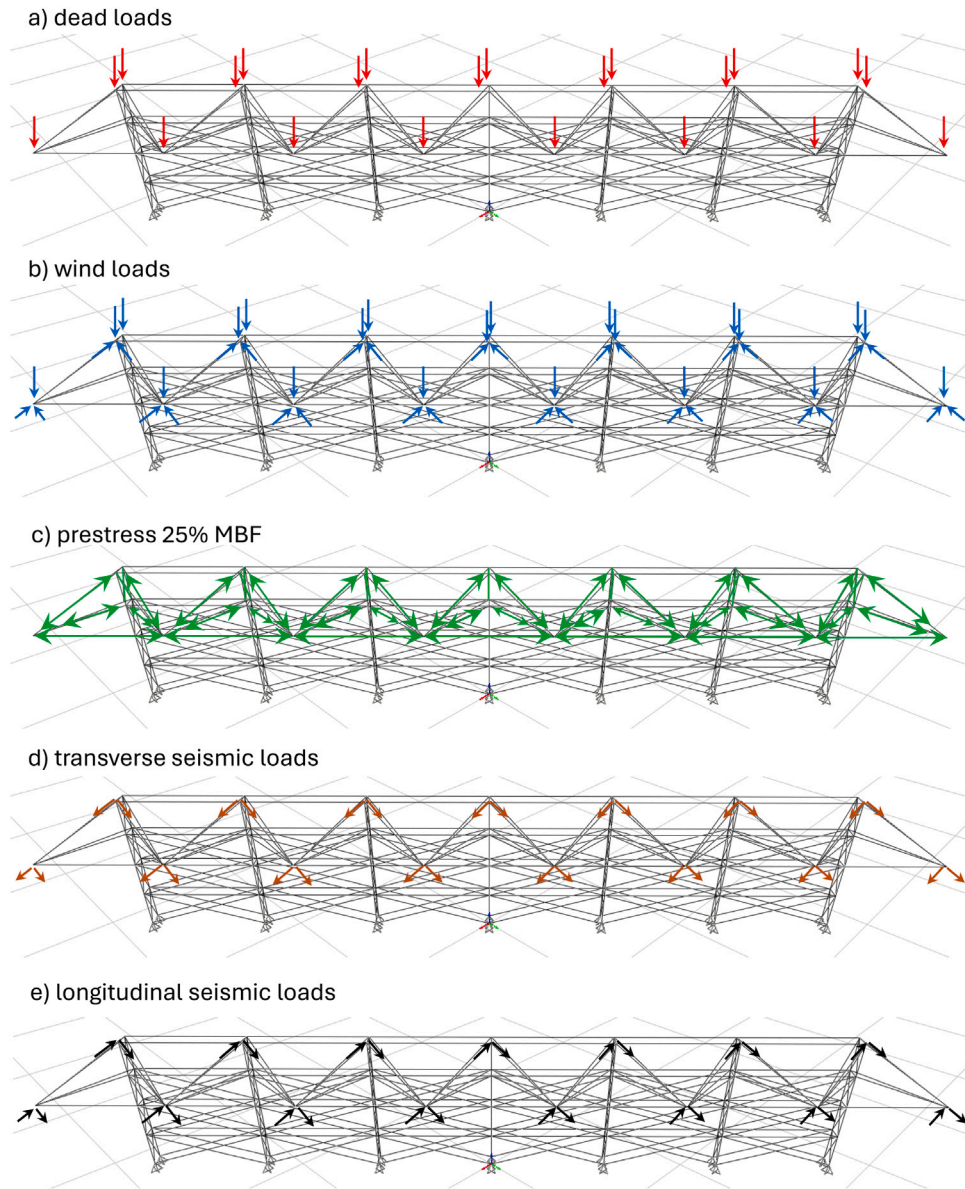
Fig. 11. Illustration of the nodal forces applied under various load combinations in the finite element analysis. The boundary conditions employed include pinned joints at the base of the structure and rotational releases at both ends of all members.

utilized the Linear Buckling Analysis feature in SAP2000®, solving the following eigenvalue problem

$$\left(\mathbf{K} - \lambda\,\mathbf{K}_G\left(\boldsymbol{w}\right)\right)\mathbf{u}_\lambda = \mathbf{0}. \tag{4}$$

Here, $\mathbf{K}$ is the global stiffness matrix, while $\mathbf{K}_G$ represents the geometric stiffness matrix, which depends on the current load vector $\boldsymbol{w}$ (see [31], Chap XVIII). The load multiplier λ is referred to as the Buckling Load Factor (BLF) in the remainder (i.e., an eigenvalue of problem (4)), while the corresponding eigenvector $\mathbf{u}_\lambda$ is referred to as the associated buckling mode. The BLF can be regarded as the scale factor of the load vector $\boldsymbol{w}$ that causes buckling in the given mode (i.e., a safety factor for global buckling).

Fig. 15 and Table 6 show the BLF and selected modes for the DULS, WULS, and SULS load combinations in the presence of prestress. The examined SULS load combination corresponds to $c_x = -1$ and $c_y = -0.3$ in Table 4, which was found to produce the minimum BLF values among the SULS combinations. We obtained BLFs for the first buckling mode ranging from 6.571 (WULS) to 24.289 (SULS). Notably, the BLFs are significantly greater than one, indicating that the ULS combinations

Table 6
Buckling Load Factors (BLF) for the considered load combinations under dead loads (DULS), wind loads (WULS), and seismic loads (SULS with $c_x = -1$ and $c_y = -0.3$) in the presence of prestress.

mode	DULS	WULS	SULS
1	8.216	6.571	24.289
2	25.128	20.667	40.515
3	36.274	23.692	62.195

analyzed in Section 4.1 are safe with respect to global buckling phenomena. However, a comparison of this safety assessment with those presented in Section 4.1 suggests that global buckling analysis must be carefully considered in the design of the current structures.

4.3. Pushover analysis for increasing wind loads

We conducted a nonlinear pushover analysis for increasing seismic loads, considering the load condition $1.3G + 1.5\,\lambda W$, for both the case without prestress in the cables and the case with prestress forces in the
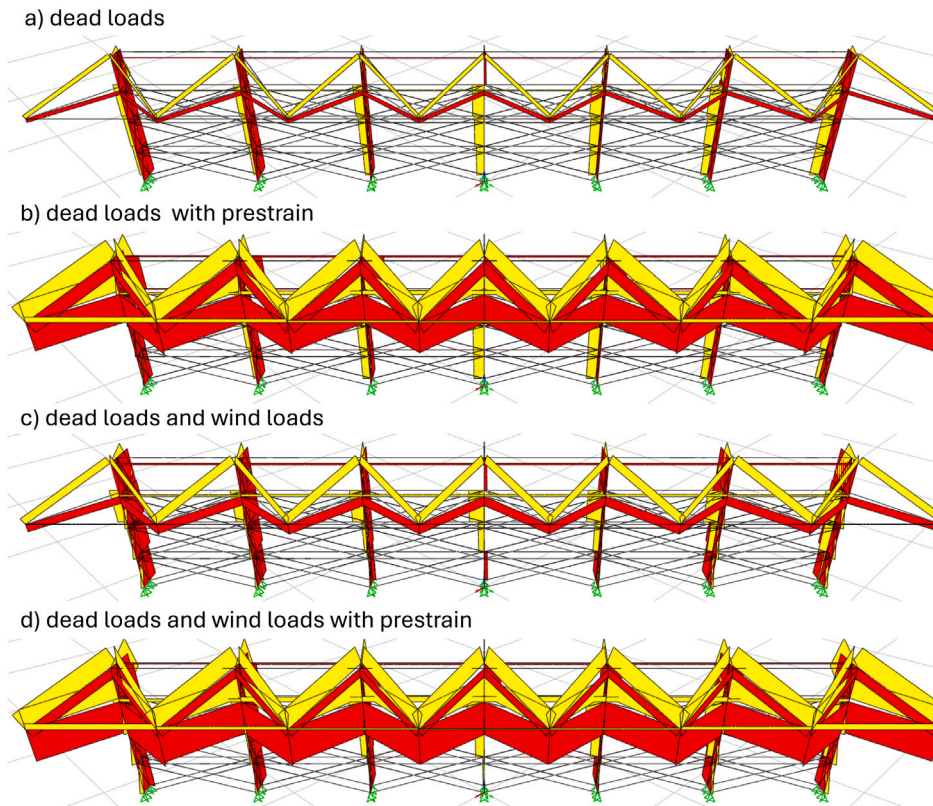
a) dead loads

b) dead loads with prestrain

c) dead loads and wind loads

d) dead loads and wind loads with prestrain

Fig. 12. Distributions of axial forces for DULS and WULS combinations. The maximum compressive axial force is $1819 \, \text{kN}$ in absolute value (reached in the bar 3–1 of the mid V-Expander module for the WULS load combination with prestress), while the maximum tensile force is $1581 \, \text{kN}$ (reached in the cable 3–2 of the same module for the same load combination).

pivot cables equal to 25% of the MB. Here, λ is a load multiplier that is increased until the structure fails due to the achievement of the ultimate strain in the plastic regime of the bars and/or cables. As anticipated, the study presented in this section employs a FE model equipped with nonlinear link elements that carry only axial forces for the bars and cables. These elements exhibit a nonlinear, elastic-perfectly-plastic relationship between axial force and axial displacement. For the cables, we assume a maximum compressive force of zero (tension-only response), while for the bars, we assume that the maximum allowable compressive force is the lesser of the yielding and buckling loads. In the presence of prestress, a slightly different model is analyzed, replacing the link members of the cables with the prestrained cable elements available in SAP2000® [31], which exhibit the same constitutive response defined above. The pushover analysis accounts for large displacement effects through the formulation of the equilibrium equations for the structure in its deformed configuration.

Fig. 16 shows the pushover curves relating the total vertical force at the base of the examined grandstand structure (summation of the vertical forces acting at the base of all the columns) with the vertical deflection of the most deformed module ('displacement of control node'). It can be observed that the application of prestress produces a 47% increase in the initial slope of the pushover curve, which rises from $32.4 \, \text{kN} \, \text{mm}^{-1}$ to $47.6 \, \text{kN} \, \text{mm}^{-1}$, and a 39% increase in the maximum base force, which rises from $10\,573 \, \text{kN}$ to $14\,743 \, \text{kN}$. It is also observed that the WULS load combination corresponds to points on the linear branches of the pushover curves. These points occur at total base forces significantly lower than those associated with the first bending point of the pushover curve, indicating that the structure responds in the linear-elastic regime under such a load combination.

4.4. Pushover analysis for increasing seismic loads

A pushover analysis was conducted also in presence of increasing seismic forces, using the FE model that has been illustrated in the previous section. The load conditions $G + P + \lambda_x E_x$ (transverse seismic forces) and $G + P + \lambda_y E_y$ (longitudinal seismic forces) were analyzed, accounting for large displacement effects. Here, λ_x and λ_y are two load multipliers associated with the transverse and longitudinal seismic loading conditions, respectively. Figs. 17 and 18 show the pushover curves relating the total base shear forces (the sum of the $x-$ or $y-$shear forces acting at the base of all the columns) to the horizontal displacements of the most deformed modules ('displacements of control nodes'). In this case, the most deformed modules were found to coincide with the mid-span V-Expander units. From the results shown in Fig. 17, it can be observed that the application of prestress significantly increases the effective ductility ratio of the structure under longitudinal seismic forces. This ductility parameter is defined as the ratio between the control displacement at failure and the control displacement at the first bending point. An 83% increase in the ductility ratio (from 1.8 to 3.3) is observed when comparing the pushover curve with prestress to the pushover curve without prestress in Fig. 17.

An even more pronounced increase in the effective ductility ratio is observed in the pushover curves shown in Fig. 18. Here, the ductility ratio is 1.3 without prestress and increases to 6.2 with prestress, representing a 377% increase. It is worth noting that the points corresponding to the load conditions $G + E_y$ ($\lambda_y = 1$) and $G + E_x$ ($\lambda_x = 1$) lie on the linear branches of the pushover curves, positioned very close to the origin and far from the first bending point. This is also true for the SULS combinations, replicating what we observed under the WULS combination.

5. Solar energy harvesting capacity

We now proceed to estimate the solar energy harvesting capacity of the stadium roof examined in this study (Section 3), using the geographical coordinates of Salerno, which were previously employed
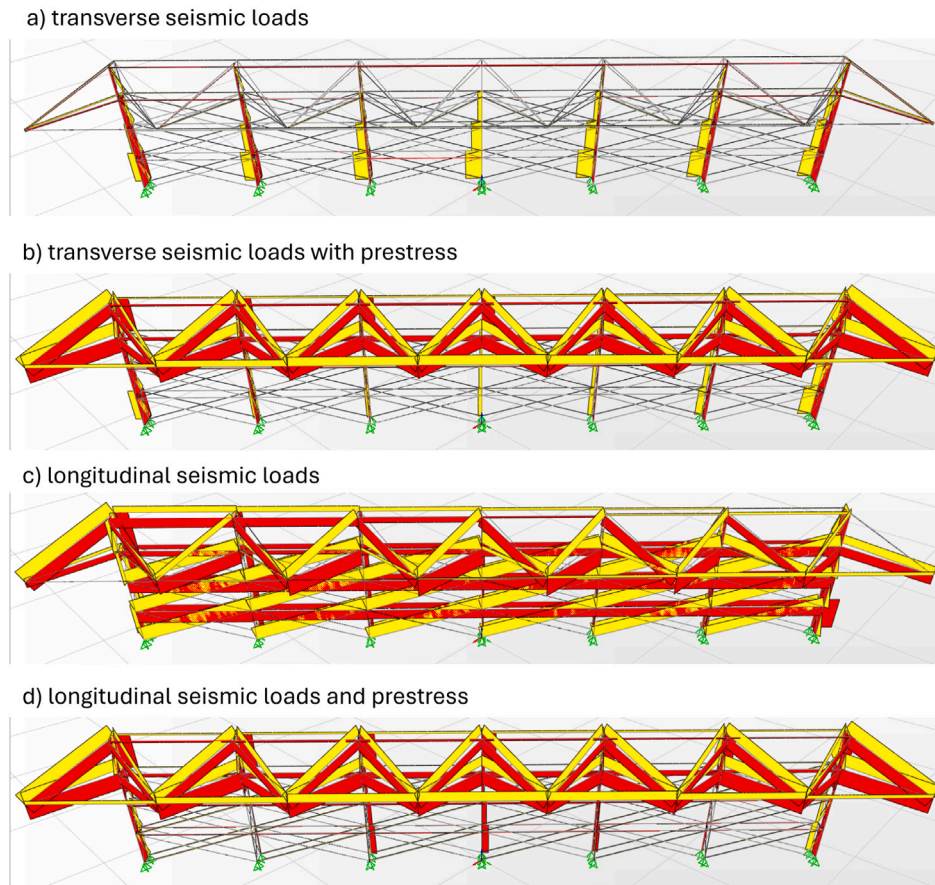
a) transverse seismic loads

b) transverse seismic loads with prestress

c) longitudinal seismic loads

d) longitudinal seismic loads and prestress

Fig. 13. Distributions of axial forces for selected SULS combinations. Under such combinations, the maximum compressive axial force is 1709 kN in absolute value (reached in the bars 3–1 of the terminal V-Expander modules for the load combination with longitudinal seismic forces and prestress), while the maximum tensile force is 1168 kN (reached in the cables 3–2 of the penultimate V-Expander modules for the same load combination).

a) WULS without prestress

b) WULS with prestress
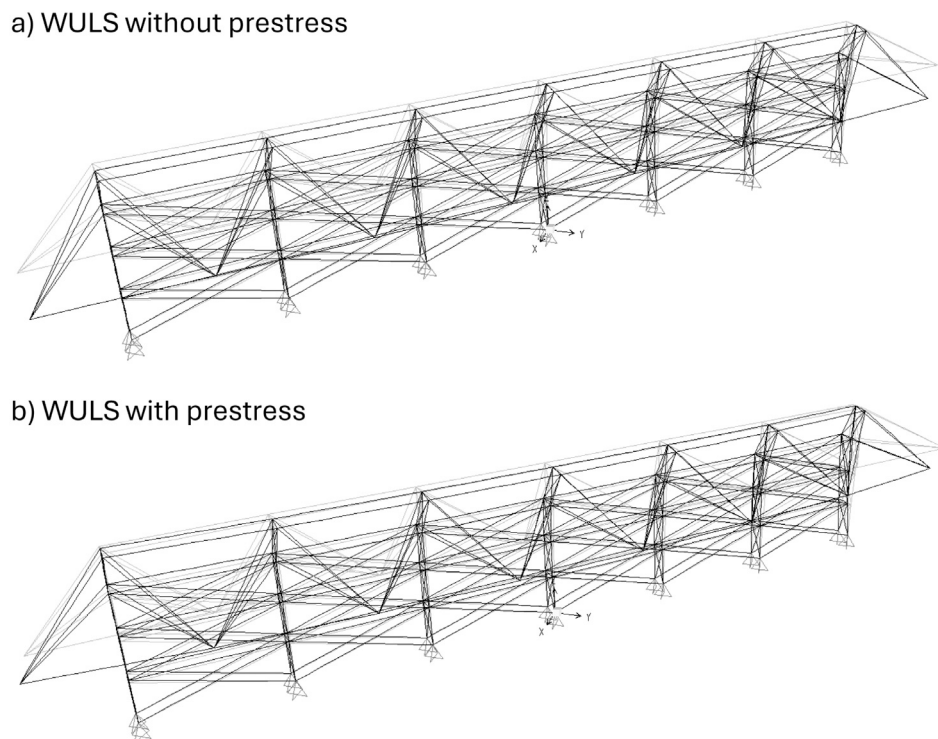
Fig. 14. Deformed shapes under WULS load combinations. Displacement magnification factor equal to 60 applied.

a) DULS – mode 1 (BLF = 8.216)
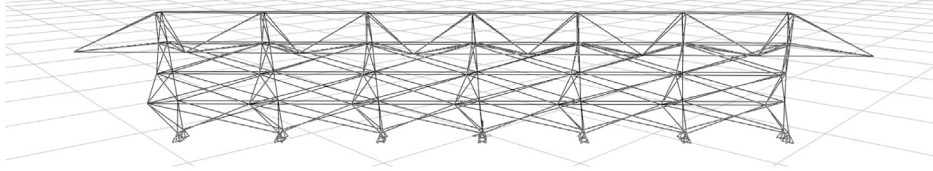
b) WULS – mode 1 (BLF = 6.571)
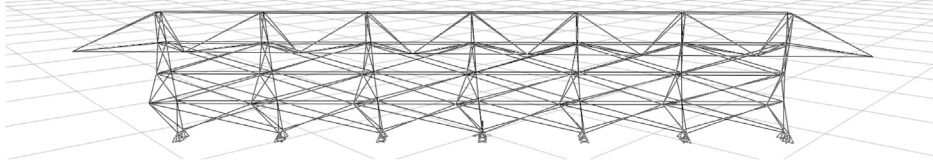
c) SULS (c_x = -1 , c_y = -0.3) – mode 1 (BLF = 24.289)
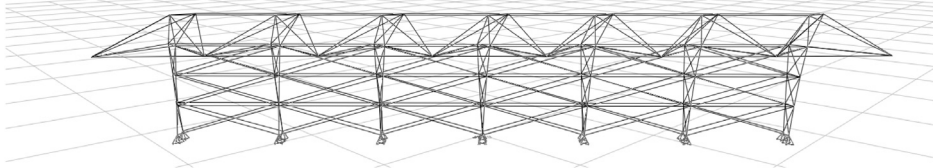
Fig. 15. First buckling modes and corresponding buckling load factors (BLF) for the considered load cases under dead loads (DULS), wind loads (WULS) and seismic loads (SULS with $c_x = -1$ and $c_y = -0.3$), in the presence of prestress.
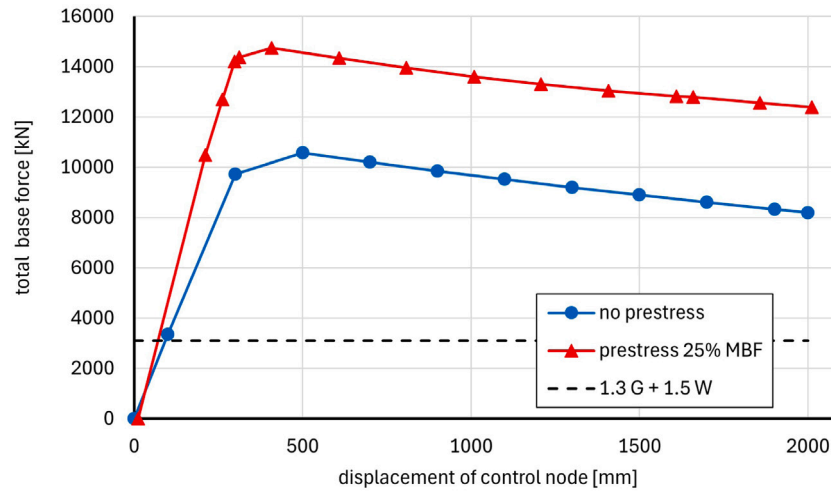
Fig. 16. Pushover curves for increasing wind loads.

for the structural analysis presented in Section 4. We analyze sun path and solar irradiance data for twelve days, one per month in 2023. These days include the vernal (spring) and autumnal equinoxes (March 20 and September 23, respectively) and the summer and winter solstices (June 21 and December 21). The remaining eight days correspond to the 15th of each of the other months. The sun path and solar irradiance data for the examined days were obtained using PVLib v0.10.3, a Python toolbox designed to simulate the performance of photovoltaic (PV) systems [37]. Our computations utilize the two reference systems illustrated in Fig. 19(a). The first is a celestial coordinate system (φ_s, ψ_s), referred to as the 'horizontal coordinate system', which uses the elevation (or altitude) angle φ_s, measured from the observer's local horizon plane, and the azimuth angle ψ_s. The second is a Cartesian coordinate system (x, y, z), where x points south, y points east and the x–y plane coincides with the local horizon plane.

Since our goal is to optimize the tilting angles of the roof panels to maximize the harvested solar energy, it would be desirable to align the unit vector normal to the roof panels, $\mathbf{n}_p$, with the unit vector in the direction of the sun rays, $\mathbf{n}_s$ (see Fig. 19(a)). Using the relationship between spherical and Cartesian coordinates [38], we can express $\mathbf{n}_s$ in the following form

$$\boldsymbol{n}_s = \begin{pmatrix} -\cos \varphi_s \cos \psi_s \\ \cos \varphi_s \sin \psi_s \\ \sin \varphi_s \end{pmatrix}. \tag{5}$$

It is well known that direct normal irradiance (DNI) constitutes the majority of global irradiance (more than 90% of global irradiance, which also includes diffuse horizontal irradiance and ground-reflected irradiance [39]). For simplicity, this study focuses exclusively on solar energy harvesting related to DNI, aiming to provide a conservative
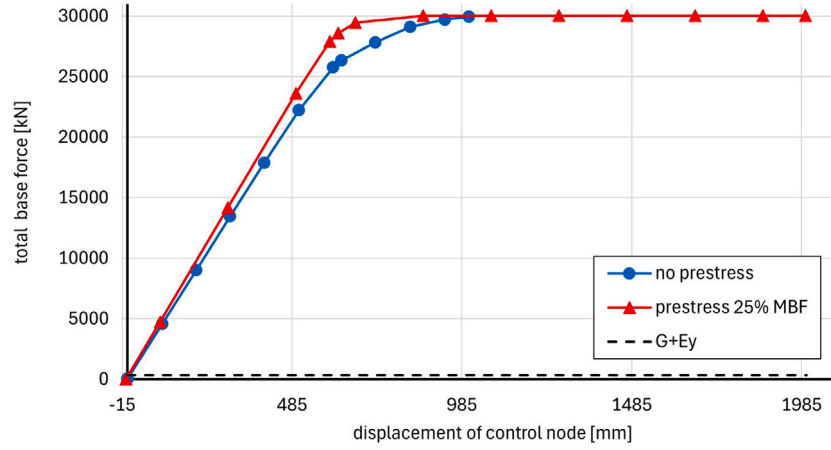
Fig. 17. Pushover curves for increasing seismic forces acting in the longitudinal direction.
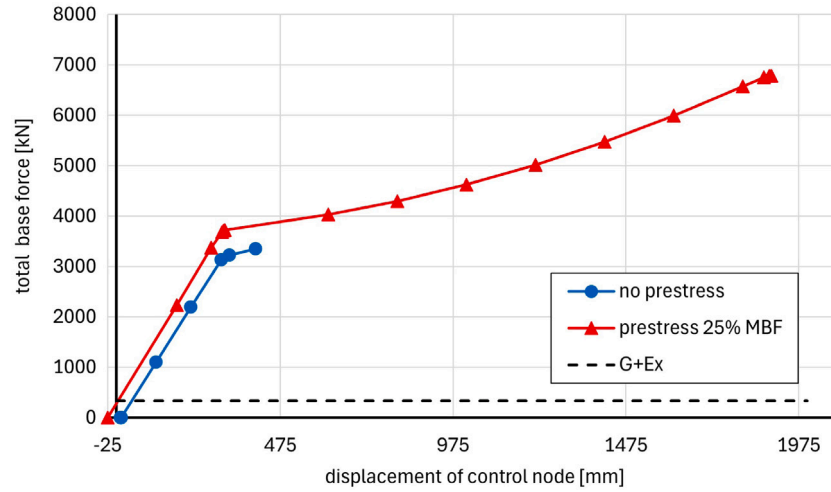

Fig. 18. Pushover curves for increasing seismic forces acting in the transverse direction.

estimate of the solar energy harvesting capacity of the stadium's solar roof. It is worth noting that this optimistic evaluation does not account for the effects of shadowing due to clouds or irradiance attenuation caused by dirt and other materials settling on the structure's surface. Conversely, incorporating other components of global irradiance would allow for the computation of energy production if bifacial photovoltaic cells were integrated into the structure instead of monofacial ones. While the self-weight of bifacial modules would remain unchanged, their power production would likely increase, especially as the tilt angle ϑ shown in Fig. 8 is increased.

DNI data for the site of Salerno were obtained using the clear sky model [40,41] available in PVLib Python [37], for each of the twelve reference days. For clarity, the hourly variation of DNI, measured in W m^{-2}, is shown in Fig. 20(a) for the equinox and solstice days only.

The input power $P_{b,in}^p$ on the solar roof covering the pth grandstand section ($p = 1, \ldots, 4$) can be estimated as

$$P_{b,in}^p(\hat{\vartheta}^p) = I_{b,n} A_b^p \mathbf{n}_s \cdot \mathbf{n}_p(\hat{\vartheta}^p) \tag{6}$$

where $I_{b,n}$ denotes the DNI, $\hat{\vartheta}^p$ is the secondary tilting angle of the solar roof, A_b^p is the direct-beam-illuminated area of the PV strips, $\mathbf{n}_p$ is the normal vector to the roof panels forming that grandstand section, and $\mathbf{n}_s$ is the above defined unit vector in the direction of the sun rays.

Based on the design presented in Section 3, we can approximately assume that A_b^p is 90% of the total area of the roof panels covering the current grandstand section. The total surface area of the roof panels covering the four grandstands of the stadium is approximately $3700 \, \text{m}^2$

($3677.09 \, \text{m}^2$).

As anticipated, we aim to maximize the scalar product $\mathbf{n}_p \cdot \mathbf{n}_s$, i.e., the cosine of the angle between $\mathbf{n}_p$ and $\mathbf{n}_s$. Due to the adopted sun-tracking strategy, which requires all roof panels of each grandstand section to be tilted at the same secondary tilting angle (see Fig. 9), it is obviously not possible for this quantity to be equal to one at all times. Therefore, we address the maximization problem of the total input energy given by

$$P_{in}(\hat{\vartheta}^1, \ldots, \hat{\vartheta}^4) = \sum_{p=1}^{4} P_{b,in}^p(\hat{\vartheta}^p) \tag{7}$$

under the constraints $0 \leq \hat{\vartheta}^p \leq \bar{\vartheta}_{max}$ ($p = 1, \ldots, 4$). It is worth remarking that $\hat{\vartheta}^p$ represents the secondary tilting angle relative to the reference configuration of the solar roof, measured about the posterior longitudinal axis. In the reference configuration, the solar roof is tilted at $\vartheta_0 \approx 30°$ about the frontal longitudinal axis (cf. Fig. 8). We safely assume $\bar{\vartheta}_{max} = 115°$, in place of the theoretical value $\hat{\vartheta}_{max} \approx 119°$, reported in Section 3. We maximize P_{in}, as defined by Eq. (7), at discrete times using the NMaximize function in *Mathematica*® 13.2, with MaxIterations set to 200, thereby obtaining an optimally-tilted configuration of the stadium roof. Next, we compute the output electrical power as

$$P_{out} = \eta \, P_{in} \tag{8}$$

where η is the PCE of the adopted PV cells. The configurations of the roof panels for the different grandstands are adjusted 12 times per hour
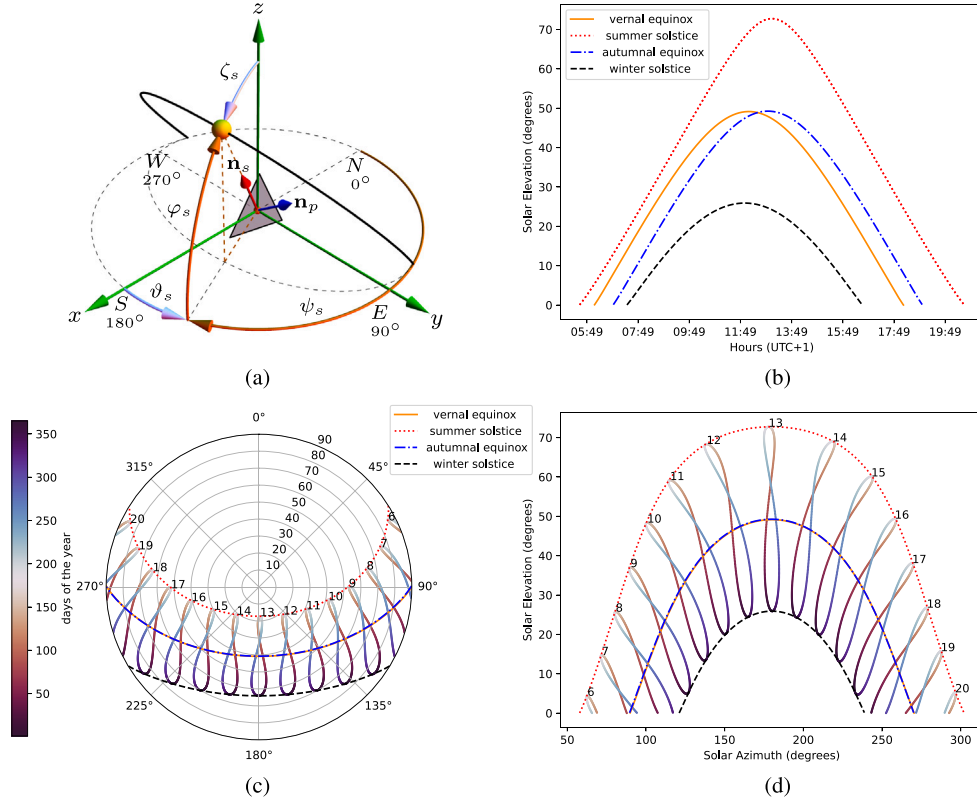
Fig. 19. Predictions of sun paths in Salerno during the equinoxes and solstices of 2023: (a) A graphical representation of the adopted coordinate systems. Here, the angle ζ_s is complementary to φ_s, and ϑ_s is supplementary to ψ_s. The vectors $\mathbf{n}_s$ and $\mathbf{n}_p$ represent unit vectors along the sun ray and the normal to the tilted roof configuration, respectively; (b) Solar elevation versus time on equinoxes and solstices; (c) Sun paths and solar analemma plots illustrating hourly variations of zenith and azimuth angles in polar coordinates; (d) Sun paths and solar analemma plots displayed in Cartesian coordinates. Hours are given in local time (UTC+01:00).
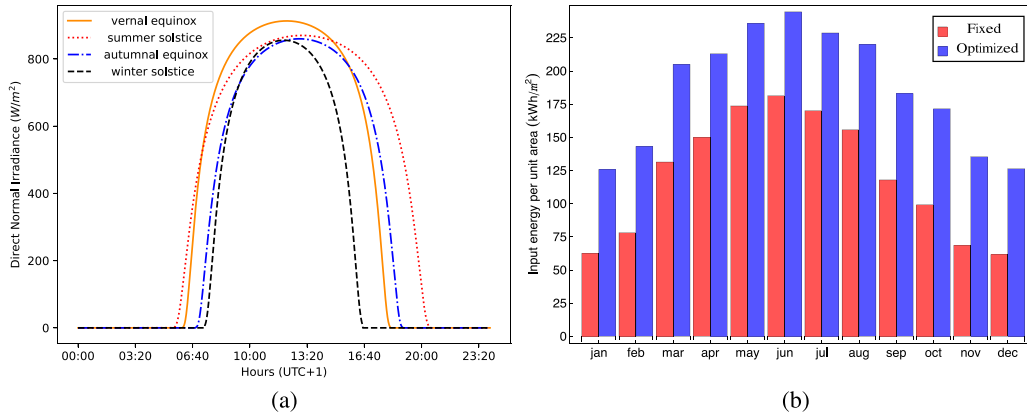
Fig. 20. (a) Hourly variation of direct normal irradiance on the reference days at the site of Salerno. Hours are given in local time (UTC+01:00). (b) Bar chart comparing the monthly input energy per unit area for the fixed slope configuration with $\hat{\vartheta} = 0$ (red bars), and the optimally tilted configuration (blue bars) of the solar roof panels.

(an adjustment every five minutes) during daylight hours on the twelve examined days at the Salerno site. It is worth calculating the input power per unit area for the entire stadium roof at a given time using the equation

$$p_{in,day} = \frac{\sum_p P_{in}^p A_b^p}{\sum_p A_b^p} \tag{9}$$

and the input solar energy per unit area for a given day through

$$e_{in,day} = \int_{t_{sr}}^{t_{ss}} p_{in,day}\,\mathrm{d}t \tag{10}$$

where t_{sr} and t_{ss} represent the sunrise and sunset times, respectively. The input solar energy that can be harvested per unit area in a given

month ($e_{in,month}$) can be roughly estimated by multiplying the $e_{in,day}$ of the reference day for that month by the number of days in the month. Fig. 20(b) compares the monthly estimates of input solar energy for the twelve months of 2023, computed using this approach. The plots in Fig. 21 instead show the variation of input power per unit area during the daylight hours of the solstices and equinoxes, as well as the variation of the DNI during the same hours.

Let us now compare the total output power of the entire stadium in the fixed-slope configuration with that in the optimally tilted configuration. The peak values, $\hat{P}_{out}$, of P_{out} estimated for the twelve reference days are shown in Fig. 22, which highlights that the maximum $\hat{P}_{out}$ occurs on the summer solstice. For $\eta = 6\%$, we predict that on this
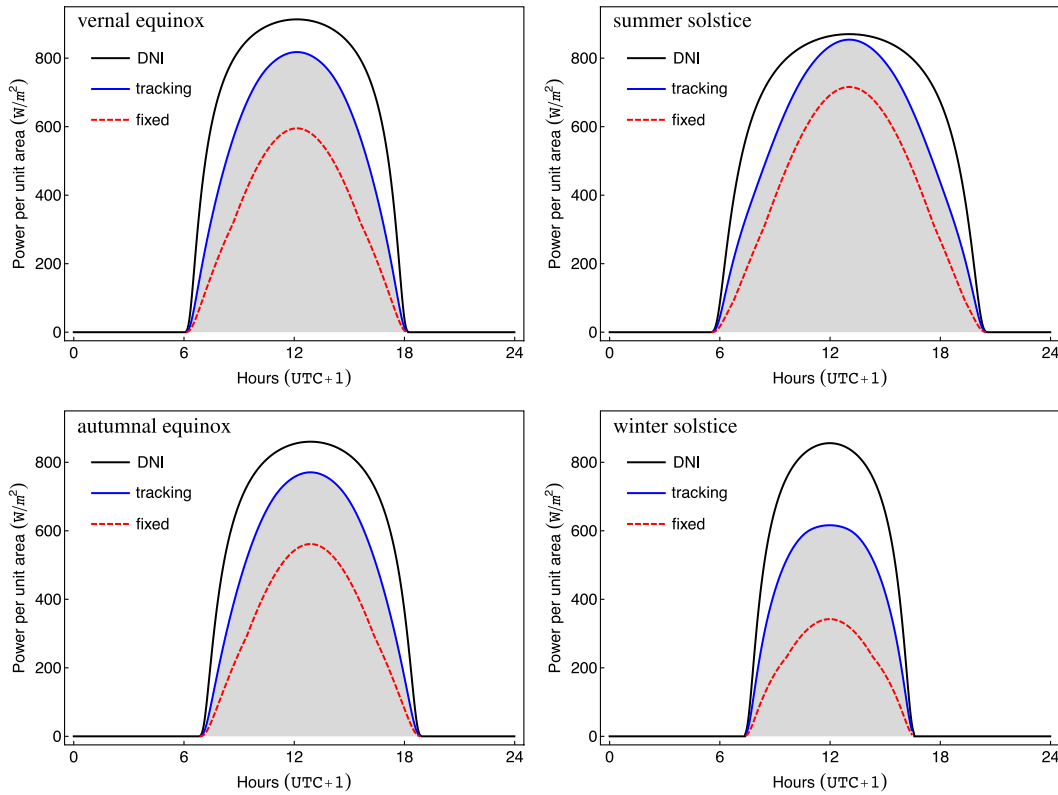
Fig. 21. Plots showing the input power per unit area for the fixed-slope configuration, the input power per unit area for the optimally tilted configuration, and the DNI at different times during the equinoxes and solstices. The gray-shaded areas represent the input solar energy per unit area on the selected days.
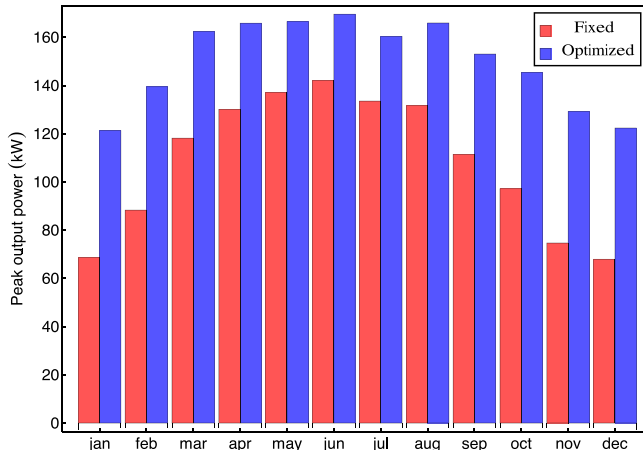

Fig. 22. Peak values of P_{out} in the reference days for the fixed-slope and the optimally-tilted roofs and $\eta = 6\%$.

day, $\hat{P}_{out} \approx 170\,\text{kW}$ with the optimally tilted configuration, compared to $142\,\text{kW}$ with the fixed-slope configuration. For $\eta = 18\%$, we predict $\hat{P}_{out} \approx 510\,\text{kW}$ with the optimally tilted configuration, compared to $426\,\text{kW}$ with the fixed-slope configuration. Finally, for $\eta = 24\%$, we predict $\hat{P}_{out} \approx 680\,\text{kW}$ with the optimally tilted configuration, compared to $568\,\text{kW}$ with the fixed-slope configuration.

Regarding the other selected days, the lowest values of $\hat{P}_{out}$ were observed in January for the optimally tilted configuration ($121\,\text{kW}$, $363\,\text{kW}$ and $484\,\text{kW}$ for $\eta = 6\%, 18\%$ and 24%, respectively) and in December for the fixed-slope configuration ($68\,\text{kW}, 204\,\text{kW}$ and $272\,\text{kW}$ for $\eta = 6\%, 18\%$ and 24%, respectively). Table 7 presents the secondary tilting angles $\hat{\vartheta}$ of the roof panels covering the north (N), south (S),

east (E), and west (W) sections of the grandstands, corresponding to the times when $\hat{P}_{out}$ is recorded on the selected days of the year. The results in this table show that the proposed sun-tracking strategy produces different secondary tilting angles in different grandstand sections, with significant differences between the angles of individual sections. The W panels exhibit large $\hat{\vartheta}$ angles, while the E and S panels maintain nearly constant secondary tilting angles of $\hat{\vartheta} \approx 30°$, at the times of $\hat{P}_{out}$, throughout the year. In contrast, the N panels display nonzero $\hat{\vartheta}$ values at the peak power time only during the May–July period. These results can be attributed to the W panels having the least favorable initial exposure during peak power times, while the N panels (initially facing south) benefit from the most favorable initial exposure. Meanwhile, the E and S panels achieve their optimal exposure in an approximately horizontal configuration at peak power time ($\hat{\vartheta} \approx 30°$; see Fig. 8). The adopted sun-tracking strategy does not permit the N panels to undergo additional frontal tilting, as previously noted. This limitation explains why these panels, especially during the times of $\hat{P}_{out}$, consistently maintain low values of $\hat{\vartheta}$ throughout the year. It is known, indeed, that for an optimized installation of PV panels in the Regione Campania of Italy (which includes the city of Salerno), the frontal tilting angles should range from 25.8° in summer to 55.8° in winter [42]. It is also worth noting that all panels exhibit nonzero secondary tilting angles at different times of the day (see, for example, the movie provided as Supplementary Material). Both Fig. 21 and Fig. 22 provide a clear graphical illustration of how much the sun-tracking strategy outperforms the fixed-slope strategy during different periods of the year.

In the discussion that follows, we use the following formula to compute the percentage increase of a generic quantity Q when transitioning from the fixed-slope to the optimally tilted configuration

$$\iota = 100\,\frac{Q^{opt} - Q^{fix}}{Q^{fix}}. \tag{11}$$

Here, Q^{opt} represents the value in the optimally tilted configuration, while Q^{fix} represents the value in the fixed-slope configuration. We
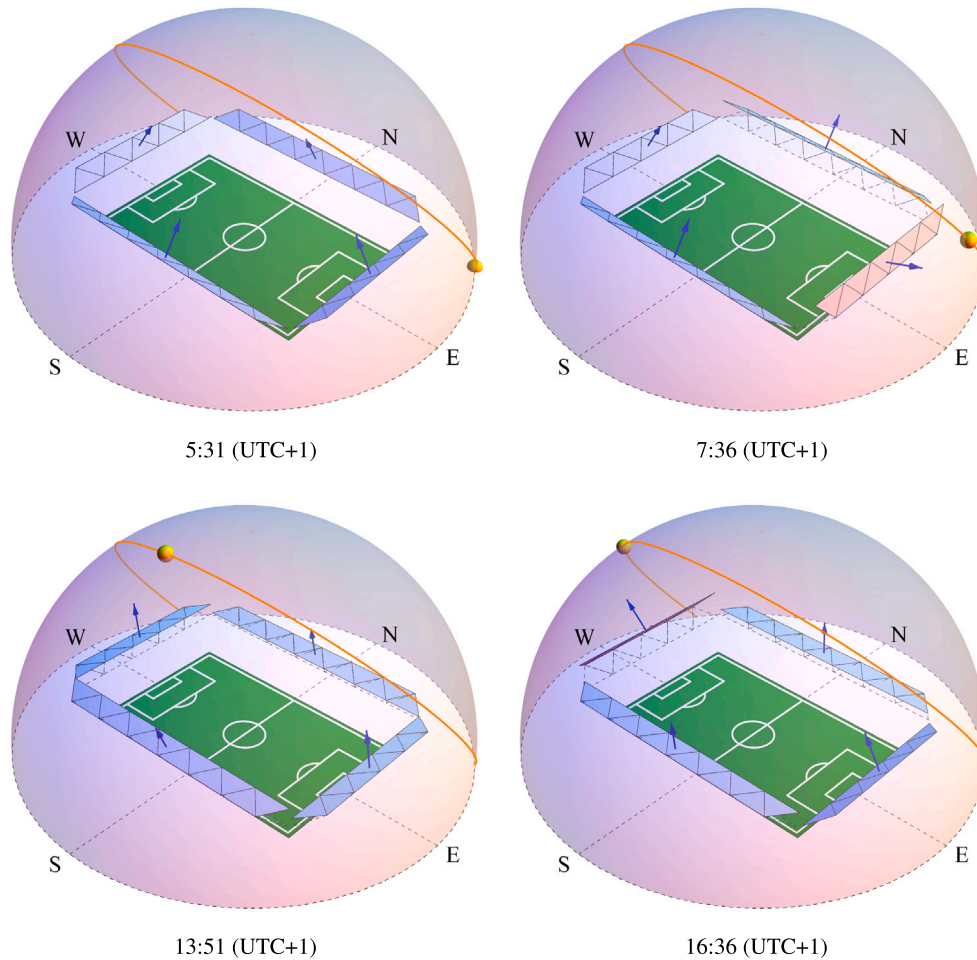
Fig. 23. Optimally-tilted configurations of the solar roof at four different hours during the summer solstice. The sun path and sun position are illustrated, along with the normal vectors to the roofs (blue arrows). The fixed-slope configuration at 5:31 (UTC+1) is taken as the reference.

Table 7
Secondary tilting angles $\hat{\vartheta}$ of the roof panels covering the north, south, east, and west sections of the grandstands, corresponding to the times when the peak power $\hat{P}_{out}$ is achieved during different months of the year.

	N	E	S	W
January	0°	32°	29°	92°
February	0°	30°	30°	84°
March	0°	30°	31°	71°
April	0°	30°	31°	61°
May	9°	31°	30°	52°
June	13°	31°	30°	48°
July	11°	30°	31°	50°
August	1°	30°	31°	60°
September	0°	30°	31°	71°
October	0°	30°	31°	80°
November	0°	30°	31°	90°
December	0°	31°	29°	95°

Table 8
Secondary tilting angles of the roof panels for the different grandstand sections corresponding to the snapshots illustrated in Fig. 23.

UTC+1	N	E	S	W
5:31	0°	0°	0°	0°
7:36	61°	99°	0°	0°
13:51	14°	19°	42°	47°
16:36	26°	0°	78°	35°

observe that the largest increases in the values of $\hat{P}_{out}$, due to the adoption of the sun-tracking strategy, occur in the months of January and December (ι = 77% and 80%, respectively), while during the summer solstice, such an increase is nearly 20%. This can be explained by the fact that, during summer, the sun is high in the sky, and therefore a fixed-slope strategy with an appropriate tilting angle performs reasonably well. In contrast, during winter, the sun is lower in the sky, making a fixed-slope strategy less efficient. Fig. 23 shows four optimally tilted configurations of the solar roof at different times on the summer solstice. This figure graphically demonstrates that the adopted

sun-tracking strategy produces distinct tilting angles for the various grandstand sections of the stadium, as previously noted. The tilting angles of the different roof panels corresponding to the snapshots in Fig. 23 are listed in Table 8.

By summing the monthly values of $e_{in,month}$, we can estimate the overall input energy per unit area for the examined year, e_{in}. We obtained an e_{in} value of $1450\,\mathrm{kW\,h\,m^{-2}}$ for the fixed-slope configuration and $2230\,\mathrm{kW\,h\,m^{-2}}$ for the optimally tilted configuration. Assuming the conservative estimate of $\eta = 6\%$, we predict that the overall solar roof of the current stadium can produce approximately $443\,\mathrm{MW\,h}$ of electrical energy (E_{out}) in one year if sun-tracking is employed, compared to about $288\,\mathrm{MW\,h}$ with a fixed-slope roof. When instead it results $\eta = 18\%$ ($\eta = 24\%$) we predict $E_{out} \approx 1328\,\mathrm{MW\,h}$ ($1771\,\mathrm{MW\,h}$) for the optimally tilted configuration and $E_{out} \approx 864\,\mathrm{MW\,h}$ ($1152\,\mathrm{MW\,h}$) for the fixed-slope configuration. This indicates that adopting the sun-tracking strategy results in a significant overall increase in electrical energy production over an entire year of approximately 54%.

6. Concluding remarks

We have presented the design of a tensegrity solar stadium roof with sun-tracking capabilities, along with the structural analysis and a study of its solar energy harvesting capacity. The structural analysis shows that the designed structure is stable in the linear-elastic regime under dead loads, wind, and seismic forces computed for the Salerno site according to Italian structural standards [32]. This is achieved with a lightweight structure for a solar stadium that exhibits remarkable stiffness properties, especially when compared to similar-sized sports stadiums not equipped with PV panels [10].

Regarding solar energy harvesting capacity, we have shown that the solar roof of the present small-to-medium-scale tensegrity stadium, with a capacity of nearly 10 000 seats, offers a remarkable peak electrical power output, reaching up to 510 kW when using thin-film solar panels with 18% power conversion efficiency (PCE) [28]. This value is approximately half of the peak power output offered by the Bentegodi Stadium in Verona, which has nearly four times the seating capacity of the current stadium (39 211 seats), and the National Stadium in Kaohsiung, Taiwan, which has more than five times the seating capacity of the tensegrity stadium (55 000 seats) [2]. This notable result is attributed to the implementation of an effective one-axis tracking strategy, which varies across the roof panels covering the different sections of the grandstands. Such an approach results in an overall 54% increase in electrical energy production over the course of a year compared to a fixed-slope configuration. The sun-tracking strategy is particularly efficient during the winter months, achieving peak power increases of up to 80%. The findings also reveal that the optimal orientations of the roof panels across the various grandstands differ significantly. This suggests that a fixed-slope design approach is not ideal for energy harvesting. Conversely, a sun-tracking strategy — an approach that, to the best of our knowledge, is uncommon in sports stadiums — offers greater flexibility in optimizing the stadium's layout and the initial slope of the PV panels.

Overall, we conclude that the tensegrity concept presented in this work for a solar stadium is highly promising, both in terms of structural response and electrical energy production. The sun-tracking strategy presented can be further optimized by allowing the individual modules forming the roofs of the grandstand sections to exhibit different tilting angles and, potentially, incorporate two-axis tracking. These topics are subjects we plan to explore in future work. Additional improvements to the solar stadium design strategy could include the adoption of high-efficiency silicon solar cells, which offer PCEs of up to 27%–28% [43], as well as the use of bifacial cells. These cells would enable the stadium to capture both diffuse and reflected irradiance components without adding extra weight. Furthermore, the tensegrity-stadium concept can be scaled up for large-scale stadiums. An advanced structural study of the supporting structures could encompass dynamic responses to wind and seismic loads [44,45], the potential tilting of roof panels under such conditions, and a nonlinear buckling analysis [10], incorporating prestress effects.

CRediT authorship contribution statement

Rana Nazifi Charandabi: Writing – review & editing, Writing – original draft, Visualization, Validation, Supervision, Software, Methodology, Investigation, Formal analysis, Data curation, Conceptualization. **Enrico Babilio:** Writing – review & editing, Writing – original draft, Visualization, Validation, Supervision, Software, Methodology, Investigation, Formal analysis, Data curation, Conceptualization. **Gerardo Carpentieri:** Writing – review & editing, Writing – original draft, Visualization, Validation, Supervision, Software, Methodology, Investigation, Formal analysis, Data curation, Conceptualization. **Giovanni Spagnuolo:** Writing – review & editing, Writing – original draft, Visualization, Validation, Formal analysis, Conceptualization. **Ada Amendola:** Writing – review & editing, Writing – original draft, Visualization, Validation, Supervision, Resources, Project administration, Methodology, Investigation, Funding acquisition, Formal analysis, Data curation, Conceptualization. **Fernando Fraternali:** Writing – review & editing, Writing – original draft, Visualization, Validation, Supervision, Software, Resources, Project administration, Methodology, Investigation, Funding acquisition, Formal analysis, Data curation, Conceptualization.

Declaration of competing interest

The authors declare that they have no known competing financial interests or personal relationships that could have appeared to influence the work reported in this paper.

Appendix A. Supplementary data

A movie illustrating the sun-tracking strategy of the solar roof during the summer solstice of the reference year is provided as Supplementary Material.

Supplementary material related to this article can be found online at https://doi.org/10.1016/j.tws.2025.113033.

Data availability

Data will be made available on request.

References

[1] PowerTechnology, Renewable stadiums of the future, 2019, https://www.power-technology.com/features/best-stadiums-renewable-energy/. (Accessed 24 November 2024).

[2] Solarplaza, Top 50 solar stadiums worldwide (2018 world cup edition), 2018, https://www.solarplaza.com/resource/11879/top-50-solar-stadiums-worldwide-2018-world-cup-edition/. (Accessed 24 November 2024).

[3] S.O. Lyu, Unveiling willingness to pay for green stadiums: Insights from a choice experiment, J. Clean. Prod. 434 (2024) 139985, http://dx.doi.org/10.1016/j.jclepro.2023.139985.

[4] E.E.L. Yaroni, Evolution of Stadium Design (Ph.D. thesis), Massachusetts Institute of Technology, 2012, (Accessed 24 November 2024).

[5] Linkedin: ESG in Sport, The FIFA world cup and sustainability, 2024, https://www.linkedin.com/pulse/fifa-world-cup-sustainability-evolving-together-fifas-120th-ujfve/. (Accessed 24 November 2024).

[6] R. Ahsan, R. Al-Abri, H. Al-Zakwani, N. Ambu-Saidi, E. Hossain, Design and economic analysis of a solar photovoltaic system for a campus sports complex, Int. J. Renew. Energy Res. (IJRER) 10 (1) (2020) 67–78, http://dx.doi.org/10.20508/ijrer.v10i1.10231.g7838.

[7] M. Manni, V. Coccia, A. Nicolini, G. Marseglia, A. Petrozzi, Towards zero energy stadiums: The case study of the Dacia Arena in Udine, Italy, Energies 11 (9) (2018) 2396, http://dx.doi.org/10.3390/en11092396.

[8] Architectuul, Kaohsiung Stadium, 2013, https://architectuul.com/architecture/kaohsiung-stadium. (Accessed 24 November 2024).

[9] Euronews, Green Galatasaray: Turkish football giant saves almost €400,000 from its solar roof, 2022, https://www.euronews.com/green/2022/10/03/green-galatasaray-turkish-football-giant-saves-almost-400000-from-its-solar-roof. (Accessed 24 November 2024).

[10] F. Tahmasebinia, E. Chen, A. Huang, J. Li, Designing lightweight stadium roofing structures based on advanced analysis methods, Sustainability 15 (4) (2023) 3612, http://dx.doi.org/10.3390/su15043612.

[11] K. Nagase, R. Skelton, Minimal mass tensegrity structures, J. Int. Assoc. Shell Spat. Struct. 55 (1) (2014) 37–48, http://dx.doi.org/10.1117/12.2044869.

[12] R. Skelton, F. Fraternali, G. Carpentieri, A. Micheletti, Minimum mass design of tensegrity bridges with parametric architecture and multiscale complexity, Mech. Res. Commun. 58 (2014) 124–132, http://dx.doi.org/10.1016/j.mechrescom.2013.10.017.

[13] R. Skelton, M. Oliveira, Tensegrity Systems, Springer, 2009.

[14] A. Micheletti, P. Podio-Guidugli, Seventy years of tensegrities (and counting), Arch. Appl. Mech. 92 (9) (2022) 2525–2548.

[15] N. Ashwear, G. Tamadapu, A. Eriksson, Optimization of modular tensegrity structures for high stiffness and frequency separation requirements, Int. J. Solids Struct. 80 (2016) 297–309, http://dx.doi.org/10.1016/j.ijsolstr.2015.11.017.

[16] W. Gilewski, J. Kłosowska, P. Obara, Applications of tensegrity structures in civil engineering, Procedia Eng. 111 (2015) 242–248, http://dx.doi.org/10.1016/j.proeng.2015.07.084.

[17] TensegrityWiki, La Plata Stadium, 2022, https://tensegritywiki.com/index.php?title=La_Plata_Stadium. (Accessed 24 November 2024).

[18] A. Fraddosio, S. Marzano, G. Pavone, M.D. Piccioni, Morphology and self-stress design of V-Expander tensegrity cells, Compos. Part B: Eng. 115 (2017) 102–116, http://dx.doi.org/10.1016/j.compositesb.2016.10.028.

[19] R. Motro, Tensegrity: Structural Systems for the Future, Elsevier, 2003.

[20] A. Fraddosio, G. Pavone, M.D. Piccioni, Minimal mass and self-stress analysis for innovative V-Expander tensegrity cells, Compos. Struct. 209 (2019) 754–774, http://dx.doi.org/10.1016/j.compstruct.2018.10.108.

[21] M. Chen, A. Fraddosio, A. Micheletti, G. Pavone, M.D. Piccioni, R.E. Skelton, Energy-efficient cable-actuation strategies of the V-Expander tensegrity structure subjected to five shape changes, Mech. Res. Commun. 127 (2023) 104026, http://dx.doi.org/10.1016/j.mechrescom.2022.104026.

[22] R. Nazifi Charandabi, Evaluation of Methods of Applying Transformation on Tensegrity Structures Based on Geometry and the Components Organization, Tabriz Islamic Art University, Faculty of Architecture & Urbanism, 2021.

[23] Sirtef Srl, Structural spiral strands, 2024, https://www.sirtef.it/en/products/steel-wire-ropes/spiral-strands-structural-spiral-strands/. (Accessed 24 November 2024).

[24] European Committee for Standardization (CEN), EN 10219-2:2019 Cold Formed Welded Structural Hollow Sections of Non-Alloy and Fine Grain Steels - Part 2: Tolerances, Dimensions and Sectional Properties, Brussels, Belgium, 2019, European Standard.

[25] Italian Ministry of Internal Affairs, DM 10/09/1986: Norme di Sicurezza Per La Costruzione E L'esercizio Degli Impianti Sportivi (in Italian), Rome, Italy, 1986, Italian Legislative Decree.

[26] European Committee for Standardization (CEN), EN 13200-1:2019 Spectator Facilities - Part 1: General Characteristics for Spectator Viewing Area, Brussels, Belgium, 2019, European Standard.

[27] I.P. Lau, E.W. Wu, The potential application of amorphous silicon photovoltaic technology in Hong Kong, 2007, Citeseer. https://citeseerx.ist.psu.edu/document?repid=rep1&type=pdf&doi=bfff5c560189a0c979a0aebc687033f51f0d296d. (Accessed 24 November 2024).

[28] EcoWatch, Thin-film solar panels (2024 guide), 2024, https://www.ecowatch.com/solar/thin-film-solar-panels. (Accessed 24 November 2024).

[29] Solbian, SunBender solar panels, 2024, https://blog.solbian.eu/en/sunbender. (Accessed 24 November 2024).

[30] F. Fraternali, J. de Castro Motta, G. Germano, E. Babilio, A. Amendola, Mechanical response of tensegrity-origami solar modules, Appl. Eng. Sci. 17 (2024) 100174, http://dx.doi.org/10.1016/j.apples.2023.100174.

[31] Computers and Structures, Inc., SAP2000: Integrated Finite Element Analysis and Design of Structures, Computers and Structures, 2016, URL https://docs.csiamerica.com/manuals/sap2000/CSiRefer.pdf.

[32] NTC 2018, D.M. 17/01/2018. Norme Tecniche per le Costruzioni (in Italian), 2017, Gazzetta Ufficiale, N. 42 Del 20/ 02/ 2018, Supplemento ordinario N. 8 42.

[33] European Committee for Standardization (CEN), EN 1993-1-1:2022 Eurocode 3: Design of Steel Structures - Part 1-1: General Rules and Rules for Buildings, Brussels, Belgium, 2022, European Standard.

[34] European Committee for Standardization (CEN), EN 1998-1:2004 Eurocode 8: Design of Structures for Earthquake Resistance - Part 1: General Rules, Seismic Actions, and Rules for Buildings, Brussels, Belgium, 2004, European Standard.

[35] Intelligent Metal Construction, Lekhwiya stadium, 2018, https://imcgulf.com/projects/lekhwiya-stadium/. (Accessed 24 November 2024).

[36] Lightweight Structures Association of Australasia (LSAA), Abdullah bin Khalifa (Lakhwiya Stadium), 2024, https://lsaa.org/projects/stadiums/490-abdullah-bin-khalifa-lakhwiya-stadium. (Accessed 24 November 2024).

[37] W. Holmgren, K. Anderson, C. Hansen, Robwandrews, M. Mikofski, A.R. Jensen, A. Lorenzo, U. Krien, Bmu, A. Driesse, C. Stark, DaCoEx, M.S. de León Peque, T. Transue, E. Luis, Kt, N. Priyadarshi, Mayudong, Heliolytics, E. Miller, M.A. Anoma, V. Guo, L. Boeman, J. Stein, S. Aneja, W. Vining, Jforbess, T. Lunel, C. Leroy, A. Morgan, pvlib/pvlib-python: v0.10.3, 2023, http://dx.doi.org/10.5281/zenodo.10412885, Zenodo.

[38] M. Spiegel, Vector analysis and an introduction to tensor analysis, in: Schaum's Outline Series of Theory and Problems, McGraw-Hill, 1959.

[39] Y. Gao, J. Dong, O. Isabella, R. Santbergen, H. Tan, M. Zeman, G. Zhang, A photovoltaic window with sun-tracking shading elements towards maximum power generation and non-glare daylighting, Appl. Energy 228 (2018) 1454–1472, http://dx.doi.org/10.1016/j.apenergy.2018.07.015.

[40] P. Ineichen, R. Perez, A new airmass independent formulation for the Linke turbidity coefficient, Sol. Energy 73 (3) (2002) 151–157, http://dx.doi.org/10.1016/S0038-092X(02)00045-2.

[41] R. Perez, P. Ineichen, K. Moore, M. Kmiecik, C. Chain, R. George, F. Vignola, A new operational model for satellite-derived irradiances: description and validation, Sol. Energy 73 (5) (2002) 307–317, http://dx.doi.org/10.1016/S0038-092X(02)00122-6.

[42] eSolare, Inclinazione dei pannelli fotovoltaici per un'efficienza ottimale (in Italian), 2024, https://esolare.it/inclinazione-dei-pannelli-fotovoltaici/. (Accessed 24 November 2024).

[43] M. Di Sabatino, R. Hendawi, A.S. Garcia, Silicon solar cells: Trends, manufacturing challenges, and AI perspectives, Crystals 14 (2) (2024) 167, http://dx.doi.org/10.3390/cryst14020167.

[44] N. Su, S. Peng, N. Hong, Analyzing the background and resonant effects of wind-induced responses on large-span roofs, J. Wind Eng. Ind. Aerodyn. 183 (2018) 114–126, http://dx.doi.org/10.1016/j.jweia.2018.10.021.

[45] A.R. Wittwer, J.M. Podestá, H.G. Castro, J.L. Mroginski, J.O. Marighetti, M.E. De Bortoli, R.R. Paz, F. Mateo, Wind loading and its effects on photovoltaic modules: An experimental–computational study to assess the stress on structures, Sol. Energy 240 (2022) 315–328, http://dx.doi.org/10.1016/j.solener.2022.04.061.